

---

# Geometric Pareto Control: Riemannian Gradient Flow of Energy Function via Lie Group Homotopy

Tong Wu

*Department of Electrical and Computer Engineering  
University of Central Florida*

*tong.wu@ucf.edu*

## Abstract

We propose Geometric Pareto Control (GPC), a framework that overcomes key barriers of reinforcement learning in cyber-physical systems where the governing physics is known. Reinforcement learning confronts fundamental barriers in safety-critical applications: sample complexity grows exponentially with action-space dimension, complete retraining is required whenever objectives or operating conditions shift, competing goals such as safety recovery and economic dispatch demand brittle mode-switching logic, and unsafe exploration persists even under constrained RL formulations. GPC resolves these barriers through a two-stage geometric approach. Offline, the supported family of Pareto-optimal solutions (i.e. solutions recoverable by weighted scalarization) is embedded as a submanifold within a Lie group. Exponential map closure preserves membership in the ambient Lie group at every step; drift and reset assumptions then keep online latent states within a bounded neighbourhood of the Pareto submanifold, and a training-time feasibility margin guarantees that all decoded actions remain feasible without post-hoc projection, analogous to constructing a "map" of the entire solution landscape. Online, a closed-form proximal navigator traverses this submanifold via a unified Riemannian gradient flow driven by a singular perturbation potential field, which induces emergent dual-timescale dynamics that automatically prioritize constraint restoration over performance optimization without explicit switching, analogous to real-time "navigation" across this map toward the contextually optimal operating point. The homeomorphic structure of the submanifold guarantees that continuously varying system parameters and objective weights produce continuously varying control actions, enabling deployment under unseen conditions and distributions without retraining. Validated on three benchmarks spanning a nonconvex analytical control task and real-time multi-objective optimal power flow (OPF) on the IEEE 30-bus network, GPC achieves 100% feasibility under both nominal and uncertain operating conditions, tracks the Pareto-optimal oracle to within 0.30% suboptimality at 12.3 ms per decision step, and adapts priority autonomously from constraint recovery to economic dispatch without mode switching. Under power system transmission branch admittance uncertainty, where network parameters are unknown but their distributions are estimated, GPC maintains 100% feasibility with no retraining while model-free baselines produce zero feasible dispatches.

## 1 Introduction

### 1.1 Background and Motivation

Over the past decade, reinforcement learning has emerged as the dominant paradigm for sequential decision-making in complex control problems Sutton et al. (1998); Arulkumaran et al. (2017); Bertsekas (2019). Driven by its ability to learn policies directly from environment interaction without requiring an explicit system model, RL has achieved remarkable success in game playing, robotic manipulation, and simulated locomotion Mnih et al. (2015); Silver et al. (2016); Recht (2019); Schulman et al. (2017); Haarnoja et al. (2018). These achievements have fueled broad enthusiasm for extending RL to real-world cyber-physical systems such as power grids Su et al. (2025), transportation systems Haydari & Yilmaz (2020); Zong et al.

---

(2025), and wireless communication systems Luong et al. (2019); Feriani & Hossain (2021). Yet the success of RL in black-box simulation environments does not transfer to white-box physical systems, where the governing physics is known, constraints are hard, and failures carry real consequences Dulac-Arnold et al. (2021).

- **Sample complexity.** Model-free RL requires an enormous number of environment interactions to learn a reliable policy Sutton et al. (1998). In cyber-physical systems, each interaction requires a full physics simulation, making the data collection process computationally prohibitive and time-consuming before any deployment can occur Kakade (2003).
- **Curse of dimensionality.** As the state-action space expands in high-dimensional CPS, the underlying search space grows exponentially and the optimization becomes intractable, making convergence within any practical time budget unachievable Lu et al. (2025). Continuous control variables across large-scale networks make exhaustive coverage of the operational envelope practically impossible, regardless of computational resources.
- **Multi-timescale mismatch.** CPS operate across fundamentally different timescales: fast safety-critical responses on the order of milliseconds and slow economic objectives on the order of minutes to hours. Standard RL formulations rely on a fixed time step and a single discount factor, making it structurally unable to handle objectives that operate across mismatched temporal horizons within a unified policy Kulkarni et al. (2016).
- **Brittleness under distribution shift.** An RL policy trained under one operating condition performs unpredictably when the environment changes, for example following a topology change, a load shift, or a fault scenario in power systems. Complete retraining is required whenever objectives or operating conditions shift, yet safety-critical CPS cannot be taken offline for this purpose Fujimoto et al.
- **Unsafe exploration and sim-to-real gap.** RL policies must explore the action space during training, which in physical systems translates directly to constraint violations, equipment damage, and cascading failures Su et al. (2025). Simulation-based training avoids physical damage but introduces a sim-to-real gap that is most severe in fault and near-limit scenarios, where heuristic reward shaping and mode-switching logic are least likely to generalize and hardest to certify.

These limitations are not engineering difficulties to be overcome with better tuning or more data Dulac-Arnold et al. (2021). They share a common root: RL treats every system as a black box, discarding the prior knowledge that is often available in practice M. Moerland et al. (2023). Many real-world systems are governed by well-characterized physical laws, structured constraints, and known dynamics Karniadakis et al. (2021). Even when system parameters are not precisely known, their distributions can often be inferred from historical operational data Chua et al. (2018); Ghahramani (2015). Exploiting this knowledge directly, rather than rediscovering it through trial and error, is the central opportunity that model-based geometric approaches offer over purely data-driven RL.

## 1.2 Related Work

We organize prior work according to the fundamental challenges. Existing approaches address these challenges only partially because they operate within fundamentally different paradigms. Reinforcement learning prioritizes adaptability but lacks safety guarantees and sample efficiency Dulac-Arnold et al. (2021). Classical optimization ensures constraint satisfaction but does not provide real-time adaptability under changing objectives and operating conditions Bertsekas (1997; 2012). Geometric and model-based methods preserve system structure but do not encode Pareto optimality or autonomous priority adaptation. As a result, existing methods lack a geometric mechanism for continuously navigating the Pareto-optimal solution space under changing system conditions.

### 1.2.1 Safe Reinforcement Learning

Constrained MDPs formalized via Lagrangian relaxation Altman (2021); Wachi & Sui (2020); Altman (1998) provide a principled framework for constraint satisfaction by augmenting the reward with penalty terms for

---

constraint violation. However, Lagrangian methods rely on soft penalties that can be violated during training, require careful tuning of multiplier update rates, and provide no guarantee that the learned policy remains feasible under distribution shift Wu et al. (2023); Su et al. (2025). Trust-region methods such as CPO Achiam et al. (2017) and its successors improve constraint satisfaction rates by restricting policy updates to a feasible neighborhood Tessler et al. (2018), but the trust region radius must be manually tuned and the method scales poorly to high-dimensional action spaces. Lyapunov-based safe RL Chow et al. (2018); Wang & Wu (2024) constructs stability certificates that provably confine the policy to a safe region, but the Lyapunov function must be specified by hand, which is intractable for complex CPS without closed-form dynamics. Control barrier functions (CBF) combined with RL Garcia & Fernández (2012); Wabersich et al. (2023); Yang et al. (2025) enforce hard instantaneous safety by projecting the RL policy output onto a safe set at execution time, providing a strong single-step guarantee. However, the safe set must be explicitly defined in state space, the projection can conflict with the policy gradient and cause oscillatory behavior near constraint boundaries, and CBFs do not extend naturally to multi-objective settings where the notion of safety itself is context-dependent. Shielding and runtime monitors Alshiekh et al. (2018); Carr et al. (2023) intercept unsafe actions at execution time and substitute a pre-specified fallback policy, providing a hard safety guarantee without modifying the learning algorithm. However, the fallback policy must be separately designed, the switching between learned and fallback behavior introduces discontinuities in the control signal, and the shield provides no guidance on efficient recovery after an intervention Garcia & Fernández (2015); Wachi et al. (2024). Collectively, safe RL methods address constraint satisfaction in isolation but leave sample complexity, distribution shift, and multi-timescale mismatch entirely unresolved.

### 1.2.2 Offline RL and Pretraining

Offline RL methods including IQL Kostrikov et al. (2021), CQL Kumar et al. (2020), and TD3+BC Fujimoto & Gu (2021) address sample complexity by learning entirely from pre-collected datasets, eliminating the need for online environment interaction during training. Behavior cloning and imitation learning further simplify this by treating the problem as supervised regression onto expert actions. Decision Transformer Chen et al. (2021) and trajectory modeling approaches reframe RL as sequence prediction over offline trajectories, enabling the use of large-scale pretraining infrastructure. Foundation models for control Janner et al. (2021); Brohan et al. (2022); Reed et al. (2022) extend pretraining to multi-task settings, demonstrating broad generalization across environments. Despite these advances, offline RL methods remain fundamentally limited by the quality and coverage of the offline dataset: distribution shift between the training data and the deployment environment leads to value overestimation and policy degradation, a problem that is most severe precisely in the rare but critical fault scenarios that matter most for safety. Fine-tuning is required whenever operating conditions change significantly, and the trained policy still provides no hard constraint guarantees at deployment time. Multi-timescale dynamics are not addressed, as all existing offline RL methods operate at a single fixed timestep.

### 1.2.3 Latent Space and Action Space Compression

Autoencoder-based action space reduction Hausman et al. (2018) and variational autoencoders Kingma & Welling (2013); Hafner et al. (2019b) address the curse of dimensionality by learning a low-dimensional latent embedding of the action space, confining policy search to a compressed manifold. This has been shown to accelerate RL convergence significantly in high-dimensional continuous control benchmarks. World models such as Dreamer Hafner et al. (2019a) and its successors Hafner et al. (2023) perform planning entirely in a learned latent space, further decoupling representation learning from policy optimization and enabling long-horizon reasoning with substantially fewer environment interactions. However, all of these approaches learn the latent space purely from data, without imposing physical constraints, Pareto structure, or continuity properties that would be needed for safe real-time deployment. The compressed space provides no guarantee that decoded actions are feasible or Pareto-optimal. Moreover, navigating the latent space at runtime still relies on a learned RL policy, inheriting its exploration requirements and brittleness under distribution shift. When the latent space is learned separately from the control objective, there is no guarantee that the geometry of the latent space is compatible with the constraint structure of the physical system.

---

### 1.2.4 Multi-Objective Optimization and Pareto Methods

Multi-objective evolutionary algorithms including NSGA-II Deb et al. (2002) and MOEA/D Zhang & Li (2007) are the classical approach to approximating the Pareto front of a multi-objective problem. These methods are population-based, derivative-free, and well-suited to nonconvex problems, but they are inherently offline: they produce a discrete set of Pareto-optimal solutions that must be computed in advance, and they provide no mechanism for real-time adaptation when the operating priority shifts. Multi-objective RL (MORL) Van Moffaert & Nowé (2014); Abels et al. (2019); Roijers et al. (2013) extends the RL framework to vector-valued rewards, training a single policy conditioned on a preference vector so that the policy can be queried for any desired trade-off at test time. While MORL provides more flexibility than evolutionary methods, it faces the same sample complexity and unsafe exploration problems as single-objective RL, amplified by the need to cover the entire Pareto front uniformly. Pareto-conditioned networks Reymond et al. (2022) and hypervolume-based methods Pirotta et al. (2015) improve coverage of the Pareto front but still require offline precomputation and do not adapt priority autonomously from real-time constraint violations. Scalarization approaches reduce multi-objective problems to a single scalar surrogate, but the mapping from scalar weights to Pareto-optimal solutions is nonlinear and non-injective, making it difficult to navigate the trade-off surface continuously at runtime.

### 1.2.5 Physics-Informed and Model-Based Methods

Physics-informed neural networks (PINNs) Raissi et al. (2019); Karniadakis et al. (2021) incorporate known governing equations as soft constraints in the training loss, improving data efficiency and physical consistency of the learned model. Differentiable simulators de Avila Belbute-Peres et al. (2018); Hu et al. (2019) enable gradient-based policy optimization through the physics model, combining the sample efficiency of model-based methods with the flexibility of neural function approximators. Neural ODEs Chen et al. (2018) and Hamiltonian networks Greydanus et al. (2019) embed conservation laws directly into the network architecture, providing stronger structural guarantees than soft loss penalties. Koopman operator methods Brunton et al. (2016); Korda & Mezić (2018) lift nonlinear dynamics into a globally linear space by learning an embedding in which the dynamics become linear, enabling the application of linear control theory to nonlinear systems. These methods represent significant progress in exploiting known physics for data efficiency and model fidelity. However, they are primarily designed for forward simulation or single-objective stabilization tasks. None of them provide a unified framework for multi-objective Pareto navigation, autonomous priority management across competing objectives, or real-time constraint enforcement under multi-timescale dynamics. The Koopman lifting in particular provides a linear dynamics model but does not encode the Pareto structure of the solution space.

### 1.2.6 Potential Fields and Singular Perturbation Control

Artificial potential field methods Khatib (1986); Koditschek (1987) provide smooth gradient-based navigation toward goal regions while generating repulsive forces near obstacles, and have been extensively applied in robotic motion planning. The appeal of potential fields lies in their simplicity and real-time computational efficiency, but classical formulations suffer from local minima and cannot handle multi-objective trade-offs or adaptive priority without manual redesign of the potential function for each scenario. Singular perturbation theory in control Chang & Howes (2012) provides a rigorous framework for analyzing and designing controllers for systems with multiple well-separated timescales, decomposing the full system into fast and slow subsystems that can be designed independently. Barrier function methods in model predictive control Garcia et al. (1989); Ames et al. (2019) enforce hard state and input constraints via interior penalty terms, guaranteeing recursive feasibility under mild conditions. These classical tools each address an individual aspect of the problem: smooth navigation, timescale separation, or constraint enforcement. However, they are not integrated with learned manifolds, they do not generalize across objective trade-offs without manual redesign, they require expert-specified potential parameters for each new operating scenario, and they do not scale to the high-dimensional latent spaces needed for complex CPS.

---

### 1.2.7 Geometric and Riemannian Methods

Riemannian optimization Absil et al. (2008); Boumal (2023) exploits the intrinsic geometry of constraint manifolds to design gradient descent algorithms that respect the curvature of the feasible set, achieving faster convergence than projected Euclidean methods for problems with smooth manifold structure. Geodesic shooting and second-order Riemannian methods Lee (2018) extend this to trajectory optimization, enabling optimal control on curved spaces. Lie group methods in robotics and control Bullo & Lewis (2005); Murray et al. (2017); Barfoot (2024) exploit the symmetry group structure of configuration spaces to derive globally valid kinematics and dynamics representations, avoiding the coordinate singularities and chart-switching problems that arise in local parameterizations. Diffusion models on Riemannian manifolds De Bortoli et al. (2022); Huang et al. (2022) extend generative modeling to non-Euclidean spaces, demonstrating that complex distributions on curved manifolds can be learned and sampled efficiently. These works collectively establish the mathematical foundations that GPC builds upon. However, existing applications of Riemannian and Lie group methods focus on single-objective trajectory optimization, kinematic modeling, or generative modeling, rather than real-time multi-objective control. None of them address the problem of autonomously adapting objective priorities from real-time violation indicators, embedding Pareto optimality as a geometric property of the learned manifold, or providing millisecond-level deterministic computation suitable for CPS deployment.

### 1.3 Contributions

We propose Geometric Pareto Control (GPC), a geometric framework that overcomes key barriers of reinforcement learning in cyber-physical systems where the governing physics is known, even when system parameters are not precisely known but their distributions can be estimated from historical data. We summarize the principal contributions as follows:

- **Pareto map construction via Lie group embedding.** We propose an offline framework that encodes the supported family of Pareto-optimal solutions (those recoverable by weighted scalarization, covering the convex hull of the Pareto front) as a continuous, differentiable submanifold within a Lie group. Unlike evolutionary or RL-based methods that produce discrete solution sets, the manifold provides a dense, geometrically structured map of the solution landscape, with Pareto optimality guaranteed by construction rather than by penalty, resolving the sample complexity and curse of dimensionality challenges.
- **Autonomous multi-timescale navigation without mode switching.** We derive a closed-form proximal navigator that traverses the Pareto map via a Riemannian gradient flow driven by a singular perturbation potential field. The dual-timescale dynamics of fast constraint restoration and slow objective optimization emerge automatically from the potential structure, eliminating the need for explicit switching logic or manually tuned timescale parameters, directly resolving the multi-timescale mismatch challenge.
- **Autonomous priority adaptation from physical violation indicators.** We introduce a semantic coordinate system derived entirely from real-time physical violation indicators, enabling the system to shift operating priority autonomously from emergency response to economics without human intervention, predefined mode schedules, or reward shaping.
- **Provable hard constraint satisfaction through Lie group embedding.** By embedding the Pareto-optimal solution manifold within a Lie group, the exponential map closure preserves membership in the ambient group  $G$  at every integration step. Under the drift and reset assumptions (Assumptions 2–6) and the training-time feasibility margin (every point on  $\mathcal{M}^*$  lies strictly inside the feasible set), online latent states remain within a bounded neighbourhood of  $\mathcal{M}^*$ , which guarantees decoded feasibility via Proposition 2. Box constraints are enforced exactly by output clamping, and residual nonlinear constraint violations from the Lie group step decay as  $O(V_{\max}^2 \Delta t^2)$ , vanishing quadratically as the control interval shrinks.
- **Zero-shot generalization across objectives and operating conditions.** The homeomorphic structure of the submanifold guarantees that continuously varying system parameters and objective

weights produce continuously varying control actions, enabling deployment under unseen conditions and distributions without retraining.

- **Validation on real-time multi-objective optimal power flow.** We instantiate GPC on multi-objective AC OPF with multi-timescale dynamics, demonstrating enforcement of thermal and voltage constraints, Pareto-optimal dispatch tracking under continuously varying load, and autonomous priority adaptation from emergency response to economics at real-time computational cost. Under parametric system uncertainty during offline data generation, GPC learns an uncertainty-aware Pareto map that transfers zero-shot to perturbed operating conditions without online retraining, requiring only that the uncertainty distribution be estimable from historical operational data.

The remainder of this paper is organized as follows. Section 2 formulates the general constrained multi-objective dynamic optimization problem addressed by GPC. Section 3 presents the offline Pareto map construction, including dataset generation, semantic coordinate design, and the loss function system. Section 4 develops the online navigation framework, covering manifold localization, autonomous semantic target generation, nominal Riemannian gradient flow, Lie-local residual correction, and Lie group integration with retraction. Section 5 first specifies analytical navigation benchmarks with convex and nonconvex objectives, then Section 5.3 instantiates GPC on real-time multi-objective optimal power flow. Section 6 presents experimental validation. Section 7 concludes the paper. The appendix provides the RK2 predictor derivation, theoretical guarantees, proximal phase-transition integration analysis, and the forecast-induced anticipatory potential.

### Geometric Pareto Control: Riemannian Gradient Flow via Lie Group Homotopy

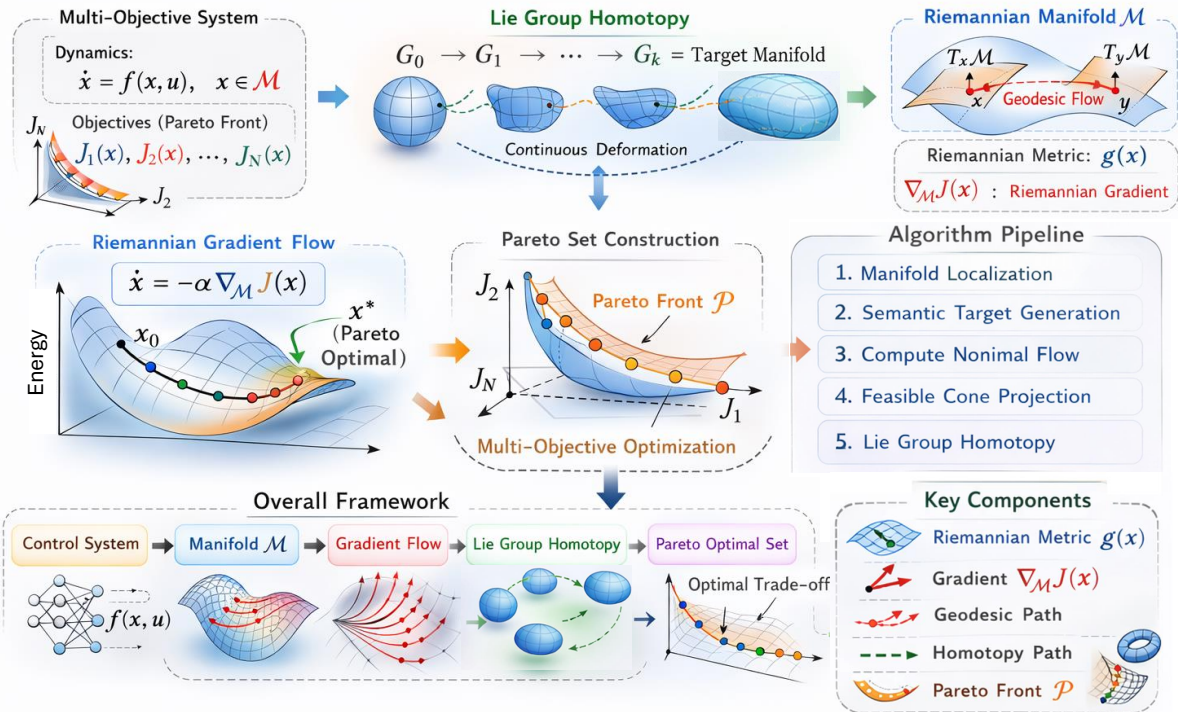


Figure 1: Overview of the proposed Geometric Pareto Control (GPC) framework. **Offline stage** (left): the supported family of Pareto-optimal solutions is embedded as a continuous submanifold  $\mathcal{M}^*$  within a Lie group via a structured encoder-decoder system trained on multi-objective optimal solutions across the operational parameter space  $\mathcal{P}$ . **Online stage** (right): a closed-form proximal navigator traverses  $\mathcal{M}^*$  via Riemannian gradient flow driven by an autonomously computed semantic coordinate  $\sigma_t$ , with hard constraint satisfaction guaranteed by Lie group neighbourhood containment combined with the training-time feasibility margin, and box constraints enforced by exact output clamping.

## 2 Background and Problem Formulation

### 2.1 Notation

Scalars are denoted by lowercase italic letters  $x \in \mathbb{R}$ , vectors by lowercase bold letters  $\mathbf{x} \in \mathbb{R}^n$ , and matrices by uppercase bold letters  $\mathbf{A} \in \mathbb{R}^{m \times n}$ . Sets are denoted by calligraphic uppercase letters  $\mathcal{X}$ , and the Lie algebra of a Lie group  $G$  is denoted  $\mathfrak{g}$ . The Euclidean and infinity norms are written  $\|\cdot\|_2$  and  $\|\cdot\|_\infty$ , respectively. The probability simplex in  $\mathbb{R}^M$  is  $\Delta^{M-1} \triangleq \{\mathbf{w} \in \mathbb{R}^M \mid \mathbf{w} \geq \mathbf{0}, \sum_{i=1}^M w_i = 1\}$ , and  $\mathcal{N}_\kappa(i)$  denotes the  $\kappa$ -nearest neighbor set of point  $i$ .

The system state, observation, control action, and exogenous disturbance at time  $t$  are denoted by  $\mathbf{s}_t \in \mathcal{S} \subseteq \mathbb{R}^{n_s}$ ,  $\mathbf{x}_t \in \mathcal{X} \subseteq \mathbb{R}^{n_x}$ ,  $\mathbf{u}_t \in \mathcal{U} \subseteq \mathbb{R}^{n_u}$ , and  $\mathbf{p}_t \in \mathcal{P} \subseteq \mathbb{R}^{n_p}$ , respectively, where  $\mathbf{s}_t$  denotes the latent physical state and  $\mathbf{x}_t$  denotes the partial observation. The latent representation is denoted by  $z \in \mathcal{Z} \subseteq \mathbb{R}^{n_z}$  with  $n_z \ll n_u$ , and  $\mathcal{M}^* \subset \mathcal{Z}$  denotes the Pareto manifold in latent space. The multi-objective cost vector is denoted by  $\mathbf{J} \in \mathbb{R}^M$ , with adaptive priority vector  $\mathbf{w}_t \in \Delta^{M-1}$  and autonomously generated semantic coordinate  $\boldsymbol{\sigma}_t \in \Delta^{M-1}$ .

The observation encoder and semantic encoder are denoted by  $E_x : \mathcal{X} \rightarrow \mathcal{Z}$  and  $E_s : \mathcal{S} \rightarrow \mathcal{Z}$ , respectively, and the action and state decoders are denoted by  $D_u : \mathcal{Z} \rightarrow \mathcal{U}$  and  $D_s : \mathcal{Z} \rightarrow \mathcal{S}$ . The action Jacobian at time  $t$  is  $\mathbf{J}_t = \partial D_u(z) / \partial z|_{z_t} \in \mathbb{R}^{n_u \times n_z}$ . The singular perturbation parameter is  $\epsilon > 0$ , and  $\Delta t$  denotes both the control timestep and the hard real-time execution deadline.

**Remark 1** (Full-State Observability Assumption). *Throughout this paper we restrict to settings where the observation function  $h : \mathcal{S} \rightarrow \mathcal{X}$  is the identity map ( $\mathbf{x}_t = \mathbf{s}_t$ ,  $\mathcal{X} = \mathcal{S}$ ), as holds in the OPF case where all bus voltages and power injections are directly measured. Under this assumption  $D_s : \mathcal{Z} \rightarrow \mathcal{S} = \mathcal{X}$ , so the observation-space residual  $\|\mathbf{x}_t - D_s(z)\|^2$  is well-defined and equals the state-space residual. Theorems stated using  $\|\mathbf{x}_t - D_s(z)\|^2$  should be understood as  $\|\mathbf{x}_t - h(D_s(z))\|^2$  for general partially observable settings, with Jacobian  $J_{h \circ D_s}$  replacing  $J_{D_s}$  throughout.*

### 2.2 Lie Groups, Riemannian Geometry, and Singular Perturbation

A **Lie group**  $G$  is a smooth manifold endowed with a group structure such that the multiplication map  $G \times G \rightarrow G$  and the inversion map  $G \rightarrow G$  are both smooth Lee (2003; 2018). The associated **Lie algebra**  $\mathfrak{g} \triangleq T_e G$  is the tangent space at the identity element  $e \in G$ , equipped with the Lie bracket  $[\cdot, \cdot] : \mathfrak{g} \times \mathfrak{g} \rightarrow \mathfrak{g}$ . The **exponential map**  $\exp : \mathfrak{g} \rightarrow G$  sends each  $v \in \mathfrak{g}$  to the endpoint at time one of the one-parameter subgroup generated by  $v$ . For any  $g \in G$  and  $v \in \mathfrak{g}$ , the left-translated update:

$$g \oplus v \triangleq g \cdot \exp(v) \in G \quad (1)$$

remains in  $G$  by the closure axiom of the group. This property is exploited in Section 4 to integrate the latent state  $z_{t+1} = z_t \oplus (\dot{z}_t \Delta t)$  while preserving membership in the ambient Lie group  $G$  by construction, without requiring a separate projection step. Neighbourhood containment of  $z_t$  around  $\mathcal{M}^* \subset G$  is a *separate* property that follows from the drift and reset assumptions stated in Appendix B; Lie group closure alone does not guarantee proximity to  $\mathcal{M}^*$ .

A **Riemannian manifold**  $(\mathcal{M}, \mathfrak{g})$  is a smooth manifold  $\mathcal{M}$  equipped with a Riemannian metric  $\mathfrak{g}$ , i.e., a smoothly varying inner product  $\mathfrak{g}_z : T_z \mathcal{M} \times T_z \mathcal{M} \rightarrow \mathbb{R}$  on each tangent space  $T_z \mathcal{M}$  Lee (2003; 2018). For a smooth function  $V : \mathcal{M} \rightarrow \mathbb{R}$ , the **Riemannian gradient**  $\text{grad}_z V \in T_z \mathcal{M}$  is the unique tangent vector satisfying:

$$\mathfrak{g}_z(\text{grad}_z V, v) = dV_z(v) \quad \forall v \in T_z \mathcal{M} \quad (2)$$

The **Riemannian gradient flow**  $\dot{z} = -\text{grad}_z V$  is the steepest descent trajectory on  $\mathcal{M}$  with respect to the metric  $\mathfrak{g}$ . Under the Łojasiewicz gradient inequality, such flows converge to a critical point of  $V$  on  $\mathcal{M}$ . Unlike Euclidean gradient descent, the Riemannian flow respects the intrinsic curvature of the manifold, ensuring that intermediate iterates remain geometrically consistent with the constraint structure.

A **homeomorphism** between topological spaces  $X$  and  $Y$  is a continuous bijection  $\varphi : X \rightarrow Y$  with continuous inverse  $\varphi^{-1} : Y \rightarrow X$  Lee (2000); Wu et al. (2026). A homeomorphism preserves all topological

invariants, including connectivity, compactness, and the fundamental group. Two spaces related by a homeomorphism are **homotopy equivalent**: there exist continuous maps  $f : X \rightarrow Y$  and  $g : Y \rightarrow X$  such that  $g \circ f \simeq \text{id}_X$  and  $f \circ g \simeq \text{id}_Y$ . In the context of GPC, the requirement that  $E_x$  induces a homeomorphism between the parameter space  $\mathcal{P}$  and the Pareto manifold  $\mathcal{M}^*$  guarantees that continuous paths in  $\mathcal{P}$  correspond to continuous trajectories on  $\mathcal{M}^*$ , a property that is enforced through the offline training procedure described in Section 3 and exploited for zero-shot generalization in Section 4.

### 2.3 Problem Statement

We consider a discrete-time, partially observed, constrained multi-objective dynamic optimization problem. The true system state  $\mathbf{s}_t \in \mathcal{S}$  evolves according to known, continuously differentiable dynamics  $\mathbf{s}_{t+1} = f(\mathbf{s}_t, \mathbf{u}_t, \mathbf{p}_t)$ , where  $\mathbf{u}_t \in \mathcal{U}$  is the control action and  $\mathbf{p}_t \in \mathcal{P}$  is an exogenous disturbance whose distribution  $\mathbb{P}(\mathbf{p})$  can be estimated from historical data. The controller does not have access to  $\mathbf{s}_t$ . Instead, it receives a partial observation  $\mathbf{x}_t = h(\mathbf{s}_t) + \boldsymbol{\eta}_t$ , where  $h : \mathcal{S} \rightarrow \mathcal{X}$  is a possibly sparse observation map with  $n_x \ll n_s$  and  $\boldsymbol{\eta}_t \sim \mathcal{N}(\mathbf{0}, \Sigma_t)$ . At deployment, control decisions must be computed using only  $\mathbf{x}_t$ .

The operator seeks to minimize  $M$  competing objectives simultaneously:

$$\mathbf{J}(\mathbf{s}, \mathbf{u}) \triangleq [J_1(\mathbf{s}, \mathbf{u}), \dots, J_M(\mathbf{s}, \mathbf{u})]^\top \in \mathbb{R}^M \quad (3)$$

subject to instantaneous physical constraints  $\mathbf{g}(\mathbf{s}_t, \mathbf{u}_t) \leq \mathbf{0}$ , temporal coupling constraints  $\mathbf{c}(\mathbf{u}_t, \mathbf{u}_{t-1}) \leq \mathbf{0}$ , and box constraints  $\mathbf{u}_t \in [\mathbf{u}^{\min}, \mathbf{u}^{\max}]$ . Let  $\mathcal{U}_t^{\text{feas}}$  denote the feasible action set at time  $t$ .

**Definition 1** (Pareto Optimality). *A feasible action  $\mathbf{u}^* \in \mathcal{U}_t^{\text{feas}}$  is Pareto-optimal if no  $\mathbf{u} \in \mathcal{U}_t^{\text{feas}}$  improves any objective without worsening another. The Pareto front  $\mathcal{F}_t^*$  is defined in the true system space, and its preimage under the decoder  $D_u$  defines the Pareto manifold  $\mathcal{M}^* \subset \mathcal{Z}$  used for real-time control.*

The objectives are ordered by timescale and safety priority:  $J_1$  encodes safety-critical violations resolved on the order of milliseconds, intermediate objectives encode quality-of-service metrics on the order of seconds to minutes, and  $J_M$  encodes economic criteria over minutes to hours. This structure induces a context-dependent priority vector  $\mathbf{w}_t \in \Delta^{M-1}$  that cannot be captured by any fixed scalarization. The contextually optimal action is defined as

$$\mathbf{u}_t^*(\mathbf{w}_t) = \arg \min_{\mathbf{u} \in \mathcal{F}_t^*} \mathbf{w}_t^\top \mathbf{J}(\mathbf{s}_t, \mathbf{u}) \quad (4)$$

where  $\mathbf{w}_t$  must be computed autonomously from the observation  $\mathbf{x}_t$ , and  $\mathbf{u}_t^*$  must be produced within a hard real-time deadline  $\Delta t$ .

**Remark 2.** *Because the system state  $\mathbf{s}_t$  is not observable at deployment, the controller must compute  $\mathbf{u}_t^*$  entirely from observation  $\mathbf{x}_t$ . This prohibits direct optimization in the true system space and necessitates a learned representation that enables real-time inference of Pareto-optimal actions from observation alone.*

**Remark 3.** *Fixed scalarization sets  $\mathbf{w}_t = \mathbf{w}$  for all  $t$ , losing adaptability to changing operating conditions. Explicit mode-switching selects among a finite set of pre-designed controllers, introducing discontinuities at switching boundaries and failing under novel constraint combinations. Iterative solvers such as IPOPT satisfy feasibility but cannot meet the real-time deadline  $\Delta t$  for large-scale systems. Geometric Pareto Control (GPC) addresses all three limitations through the latent manifold structure described in the following sections.*

## 3 Offline Stage: Pareto Map Construction

The offline stage constructs a continuous, differentiable map  $\mathcal{M}^* \subset \mathcal{Z}$  that encodes the supported family of Pareto-optimal solutions as a low-dimensional latent manifold endowed with Lie group structure. The construction proceeds in three steps: dataset generation via multi-objective optimization, semantic coordinate labeling, and manifold learning via a structured loss system.

### 3.1 Dataset Construction

The offline dataset is constructed by sampling diverse operating conditions from the parameter space and solving the multi-objective optimization problem to Pareto-optimality for each scenario.

### 3.1.1 Input-Space Sampling

Let  $\mathcal{P} \subseteq \mathbb{R}^{n_p}$  denote the disturbance or parameter space. We generate  $N$  scenarios  $\{\mathbf{p}_k\}_{k=1}^N \subset \mathcal{P}$  using Latin Hypercube Sampling (LHS), which partitions each dimension of  $\mathcal{P}$  into  $N$  equal-probability intervals and draws exactly one sample per interval. LHS guarantees uniform marginal coverage of  $\mathcal{P}$  with  $O(N)$  samples, avoiding the clustering artifacts of Monte Carlo sampling that would leave regions of the operational envelope unrepresented on  $\mathcal{M}^*$ .

### 3.1.2 Pareto-Optimal Solution Generation

For each scenario  $\mathbf{p}_k$ , the system is simulated or evaluated to obtain the corresponding true system state  $\mathbf{s}_k \in \mathcal{S}$  and partial observation  $\mathbf{x}_k = h(\mathbf{s}_k) \in \mathcal{X}$ . We then solve the multi-objective optimization problem via weighted scalarization:

$$\mathbf{u}_k(\mathbf{w}) = \arg \min_{\mathbf{u} \in \mathcal{U}_{\mathbf{s}_k}^{\text{feas}}} \sum_{i=1}^M w_i J_i(\mathbf{s}_k, \mathbf{u}), \quad \mathbf{w} \in \Delta^{M-1} \quad (5)$$

sweeping  $\mathbf{w}$  uniformly across  $\Delta^{M-1}$  to obtain diverse Pareto-optimal solutions.

**Remark 4** (Supported Pareto Points). *Weighted scalarization recovers supported Pareto-optimal solutions, i.e. points on the convex hull of the Pareto front in objective space. For problems with a nonconvex Pareto front, interior (non-supported) points are not recoverable by any positive weight vector  $\mathbf{w} \in \Delta^{M-1}$ . In such cases the dataset  $\mathcal{D}$  covers only the supported subset of  $\mathcal{M}^*$ ; claims about the completeness of the learned Pareto manifold should be understood as holding over this supported subset. For the OPF benchmarks in this work the Pareto front is empirically well-approximated by its supported points, so the distinction does not affect practical performance; users with strongly nonconvex objectives should supplement with  $\varepsilon$ -constraint or Chebyshev scalarization sweeps.*

The semantic priority coordinate  $\boldsymbol{\sigma}_k \in \Delta^{M-1}$  is computed from  $\mathbf{s}_k$  via the violation indicator framework described in Section 3.2. The dataset is:

$$\mathcal{D} = \{(\mathbf{x}_k, \mathbf{u}_k, \mathbf{s}_k, \boldsymbol{\sigma}_k, \mathbf{J}_k)\}_{k=1}^N \quad (6)$$

where  $\mathbf{s}_k$  is the true system state available only during offline data generation,  $\mathbf{x}_k$  is the partial observation available at deployment,  $\mathbf{u}_k$  is the Pareto-optimal action,  $\boldsymbol{\sigma}_k$  is the semantic priority coordinate, and  $\mathbf{J}_k = \mathbf{J}(\mathbf{s}_k, \mathbf{u}_k)$  is the objective vector.

**Remark 5** (Optional Next-Step Semantic Label). *When temporal coupling constraints are present, the dataset may be augmented to include the next-step true system state  $\mathbf{s}_{k+1}$ , from which the next-step semantic priority coordinate  $\boldsymbol{\sigma}_{k+1}$  is computed offline via the same violation indicator framework. In this case the dataset expands to:*

$$\mathcal{D} = \{(\mathbf{x}_k, \mathbf{u}_k, \mathbf{s}_k, \boldsymbol{\sigma}_k, \mathbf{J}_k, \mathbf{s}_{k+1})\}_{k=1}^N \quad (7)$$

*This captures temporal priority evolution when future safety or feasibility depends on current actions. In the absence of temporal coupling,  $\mathbf{s}_{k+1}$  is redundant and may be omitted, reducing the dataset to (6).*

**Remark 6** (Pareto by Construction). *Every sample in  $\mathcal{D}$  is obtained by solving the multi-objective problem to Pareto-optimality in the true system state space. The manifold  $\mathcal{M}^*$  is therefore implicitly defined as the encoder image of  $\mathcal{D}$ , and explicit Pareto-embedding losses or dominance penalties are unnecessary. This is a strictly stronger guarantee than enforcing Pareto optimality via a soft penalty term, which can be violated during training.*

## 3.2 Semantic Coordinate Generation

Each Pareto-optimal solution is assigned a semantic priority coordinate  $\boldsymbol{\sigma}_k \in \Delta^{M-1}$  encoding the physical urgency of the operating condition under the true system state  $\mathbf{s}_k$ , which is available during offline data generation. For each objective  $J_i$ , define a normalized violation indicator  $\delta_i(\mathbf{s}_k) \in [0, 1]$ , where  $\delta_i = 0$

indicates nominal operation and  $\delta_i = 1$  indicates the hard constraint boundary is reached. The violation indicators are mapped to urgency potentials via singular perturbation potential functions:

$$\phi_i(\mathbf{s}_k) = \exp\left(\frac{k_i \cdot \delta_i(\mathbf{s}_k)}{\epsilon_i}\right) - 1, \quad k_i > 0, \quad \epsilon_i \in (0, 1] \quad (8)$$

where  $k_i$  encodes the intrinsic priority of objective  $i$  and  $\epsilon_i$  controls the steepness of the potential wall near the constraint boundary. The semantic coordinate is obtained by normalizing the urgency potentials with a positive baseline  $\rho > 0$ :

$$\sigma_i(\mathbf{s}_k) = \frac{\phi_i(\mathbf{s}_k) + \rho}{\sum_{j=1}^M (\phi_j(\mathbf{s}_k) + \rho)} \quad (9)$$

The baseline  $\rho > 0$  prevents division by zero during nominal operation (all  $\delta_i = 0 \Rightarrow$  all  $\phi_i = 0$ ), and sets the default coordinate to the uniform point  $\boldsymbol{\sigma} = \mathbf{1}/M$  (equal economic priority) when no constraint is active. This construction ensures  $\boldsymbol{\sigma}_k \in \Delta^{M-1}$  at all times. As  $\delta_i \rightarrow 1$ , the exponential growth of  $\phi_i$  causes  $\sigma_i \rightarrow 1$  continuously (since  $\phi_i \gg \rho$  near the constraint boundary), without any threshold or rule-based switching. The semantic coordinate thus encodes a smooth, physics-driven priority ordering that transitions autonomously from economic operation to emergency response as constraint violations intensify.

**Remark 7** (Semantic-to-Geometric Translation). *During training,  $\boldsymbol{\sigma}_k$  provides supervision for the omniscient encoder  $E_s$ , anchoring the geometry of  $\mathcal{M}^*$  to the physical severity structure of the solution space. At deployment,  $\boldsymbol{\sigma}_t$  is not supplied externally; instead,  $E_x$  has learned to project the partial observation  $\mathbf{x}_t$  onto the manifold region geometrically consistent with the current violation state  $\boldsymbol{\delta}(\mathbf{s}_t)$ , enabling real-time Pareto-optimal control without explicit state estimation.*

### 3.3 Manifold Learning via Structured Loss System

The encoder-decoder system is trained on the offline dataset  $\mathcal{D} = \{(\mathbf{x}_k, \mathbf{u}_k, \mathbf{s}_k, \boldsymbol{\sigma}_k, \mathbf{J}_k)\}_{k=1}^N$  to embed the Pareto-optimal solutions onto a geometrically structured latent manifold  $\mathcal{M}^*$  via the following composite objective:

$$\mathcal{L}_{\text{total}} = \mathcal{L}_{\text{recon}}^x + \mathcal{L}_{\text{action}} + \mathcal{L}_{\text{recon}}^s + \omega_1 \mathcal{L}_{\text{consist}} + \omega_2 \mathcal{L}_{\text{local}}, \quad (10)$$

Each term addresses a distinct geometric requirement. For each sample  $(\mathbf{x}_k, \mathbf{u}_k, \mathbf{s}_k, \boldsymbol{\sigma}_k, \mathbf{J}_k) \in \mathcal{D}$ , the observation encoder and semantic encoder produce latent codes:

$$z_k^x = E_x(\mathbf{x}_k), \quad z_k^s = E_s(\mathbf{s}_k, \boldsymbol{\sigma}_k, \mathbf{J}_k) \quad (11)$$

where  $z_k^x$  is available at deployment and  $z_k^s$  is the omniscient teacher code available only during training.

**State Reconstruction ( $\mathcal{L}_{\text{recon}}^x$ ):** Forces  $z_k^x = E_x(\mathbf{x}_k)$  to encode sufficient information from the partial observation  $\mathbf{x}_k$  to reconstruct the true system state  $\mathbf{s}_k$ :

$$\mathcal{L}_{\text{recon}}^x = \frac{1}{N} \sum_{k=1}^N \|\mathbf{s}_k - D_s(z_k^x)\|^2 \quad (12)$$

**Action Reconstruction ( $\mathcal{L}_{\text{action}}$ ):** Forces  $z_k^x$  to recover the Pareto-optimal control action  $\mathbf{u}_k$  from the partial observation  $\mathbf{x}_k$  alone, which is the primary deployment objective. Applied to  $z_k^x$  only:

$$\mathcal{L}_{\text{action}} = \frac{1}{N} \sum_{k=1}^N \|\mathbf{u}_k - D_u(z_k^x)\|^2 \quad (13)$$

Applying this loss to  $z_k^s = E_s(\mathbf{s}_k, \boldsymbol{\sigma}_k, \mathbf{J}_k)$  would be trivial since  $\mathbf{u}_k$  is already recoverable from the inputs to  $E_s$  and would provide no useful gradient signal.

**Omniscient State Reconstruction ( $\mathcal{L}_{\text{recon}}^s$ ):** Forces  $z_k^s$  to encode a geometrically faithful representation of the full solution tuple  $(\mathbf{s}_k, \boldsymbol{\sigma}_k, \mathbf{J}_k)$ , providing a well-structured teacher signal for the consistency loss below:

$$\mathcal{L}_{\text{recon}}^s = \frac{1}{N} \sum_{k=1}^N \|\mathbf{s}_k - D_s(z_k^s)\|^2 \quad (14)$$

Both paths share the decoder  $D_s$ , ensuring that  $z_k^x$  and  $z_k^s$  occupy the same geometric space and are therefore directly comparable.

**Cross-Modal Consistency ( $\mathcal{L}_{\text{consist}}$ ):** Enables  $E_s$  to be discarded entirely at deployment by forcing  $E_x$  and  $E_s$  to produce coincident latent codes for the same sample  $(\mathbf{x}_k, \mathbf{s}_k, \boldsymbol{\sigma}_k, \mathbf{J}_k) \in \mathcal{D}$ :

$$\mathcal{L}_{\text{consist}} = \frac{1}{N} \sum_{k=1}^N \left[ \left( 1 - \frac{\langle z_k^x, z_k^s \rangle}{\|z_k^x\|_2 \|z_k^s\|_2} \right) + \beta \|z_k^x - z_k^s\|_2^2 \right], \quad (15)$$

The cosine term enforces directional alignment in latent space; the squared Euclidean term enforces magnitude alignment. Together they implement knowledge distillation from the omniscient teacher  $E_s$  to the physical student  $E_x$ .

**Local Structure Preservation ( $\mathcal{L}_{\text{local}}$ ):** This is the geometrically most critical term. It enforces a continuous embedding from the parameter space  $\mathcal{P}$  into the latent manifold by requiring that physically neighboring scenarios  $\mathbf{p}_k, \mathbf{p}_j \in \mathcal{P}$  map to neighboring points on  $\mathcal{M}^*$ :

$$\mathcal{L}_{\text{local}} = \frac{1}{N} \sum_{k=1}^N \sum_{j \in \mathcal{N}_\kappa(k)} \exp\left(-\frac{\|\mathbf{p}_k - \mathbf{p}_j\|^2}{\sigma^2}\right) \cdot \|z_k^x - z_j^x\|^2 \quad (16)$$

where  $\mathcal{N}_\kappa(k)$  is the  $\kappa$ -nearest neighborhood of scenario  $k$  in the parameter space  $\mathcal{P}$ . The Gaussian kernel weight decays with physical distance, concentrating the topological constraint on the most immediate neighbors. Through  $\mathcal{L}_{\text{local}}$ , the temporal continuity requirement  $\|\mathbf{u}_{t+1} - \mathbf{u}_t\| \leq \delta$  is transformed into a static geometric neighborhood relation on  $\mathcal{M}^*$ , enabling the online navigator to satisfy ramp-rate constraints through latent geometry rather than explicit enforcement.

## 4 Online Stage: Pareto Map Navigation

At deployment, the offline Pareto map  $\mathcal{M}^*$  is fixed and the online navigator operates in real time. Each control cycle consists of five steps: manifold localization from the partial observation, autonomous semantic target generation from real-time violation indicators, nominal Riemannian gradient flow via a single autograd pass, Lie-local residual correction in the decoder-pullback metric basis, and Lie group integration with optional retraction and output clamping. The entire cycle is deterministic and non-iterative, executing in milliseconds with no online solver.

### 4.1 State Estimation and Manifold Localization

At each time step  $t$ , the physical encoder produces an initial latent estimate:

$$z_{\text{obs},t} = E_x(\mathbf{x}_t) \quad (17)$$

This estimate may be corrupted by sensor noise, partial observability, or out-of-distribution inputs. Committing to a nearest-point projection onto  $\mathcal{M}^*$  is insufficient: as  $z_{\text{obs},t}$  drifts across a Voronoi boundary, the projection jumps discontinuously, producing an abrupt control transient. Instead, we admit only those manifold points that are consistent with the current observation within the sensor noise floor, defining the *measurement-consistent manifold subset*:

$$\mathcal{M}_t \triangleq \{z \in \mathcal{M}^* \mid \|\mathbf{x}_t - D_s(z)\|^2 \leq \tau_t\}, \quad \tau_t = \hat{\sigma}_t^2 + \tau_{\text{geom}} \quad (18)$$

where  $\hat{\sigma}_t^2$  is an online estimate of observation noise variance and  $\tau_{\text{geom}}$  is a geometric tolerance calibrated to the generalization error of  $\mathcal{L}_{\text{local}}$ : specifically,  $\tau_{\text{geom}}$  is set to match the empirical reconstruction residual  $\|\mathbf{x}_k - D_s(z_k^x)\|^2$  averaged over a held-out validation partition of  $\mathcal{D}$  after offline training. This calibration ensures that  $\mathcal{M}_t$  is never empty for observations drawn from the training distribution, while remaining tight enough to exclude manifold regions geometrically inconsistent with  $\mathbf{x}_t$ . The threshold  $\tau_t$  thus carries a principled two-part interpretation:  $\hat{\sigma}_t^2$  accounts for sensor noise at deployment, and  $\tau_{\text{geom}}$  accounts for the residual manifold approximation error that  $\mathcal{L}_{\text{local}}$  did not fully collapse during training. The localized state is obtained as:

$$z_t = (1 - \alpha) z_{t-1} + \alpha \arg \min_{z \in \mathcal{M}_t} \|z - z_{\text{obs},t}\|^2 \quad (19)$$

with first-order exponential smoothing ( $\alpha \in (0, 1]$ ) that suppresses high-frequency sensor noise while preserving responsiveness to genuine state changes.

## 4.2 Energy Function and Nominal Flow

The navigator’s direction of motion at each time  $t$  is determined entirely by a composite *energy function* defined on  $\mathcal{M}^*$ :

$$V(z_t, \mathbf{x}_t) = \frac{1}{\epsilon} \Phi_{\text{normal}}(z_t, \mathbf{x}_t) + \Phi_{\text{tangent}}(z_t) \quad (20)$$

No human-supplied weight vector, reference trajectory, or mode-switching logic enters this expression: both terms are built from the same physically grounded urgency potentials used to supervise the manifold during offline training, and the only runtime inputs are the partial observation  $\mathbf{x}_t$  and the current latent state  $z_t$ . Descending  $V$  produces the nominal vector field:

$$\mathbf{F}(z_t, \mathbf{x}_t) \triangleq -\nabla_z V(z_t, \mathbf{x}_t) \quad (21)$$

computed in a single autograd pass through the frozen decoders  $D_u$  and  $D_s$ . The remainder of this subsection specifies each component of  $V$ , then shows how the two terms interact to resolve the multi-timescale mismatch automatically.

**Normal potential: manifold restoration.** The normal potential measures the reconstruction residual between the current observation and the decoded manifold point:

$$\Phi_{\text{normal}}(z_t, \mathbf{x}_t) = \|\mathbf{x}_t - D_s(z_t)\|^2 \quad (22)$$

When  $z_t \in \mathcal{M}^*$ ,  $\Phi_{\text{normal}} \approx 0$ . Any off-manifold drift raises this term, generating a restoring gradient that drives  $z_t$  back onto  $\mathcal{M}^*$ .

**Tangential potential: autonomous multi-objective scalarization.** The tangential potential is the multi-objective cost scalarized by a priority coordinate  $\sigma_t(z_t) \in \Delta^{M-1}$  that is itself a function of the decoded state (not a hyperparameter supplied by the operator):

$$\Phi_{\text{tangent}}(z_t) = \sum_{i=1}^M \sigma_{t,i}(z_t) \cdot J_i(D_s(z_t), D_u(z_t)) \quad (23)$$

The priority coordinate is generated from real-time violation indicators  $\delta_i(\hat{\mathbf{s}}_t) \in [0, 1]$  evaluated on the reconstructed state  $\hat{\mathbf{s}}_t = D_s(z_t)$  (using the same definitions as Section 3.2), passed through singular-perturbation urgency potentials, and normalized via the same baseline-shifted formula as the offline stage (equation (9)):

$$\phi_i(\hat{\mathbf{s}}_t) = \exp\left(\frac{k_i \delta_i(\hat{\mathbf{s}}_t)}{\epsilon_i}\right) - 1, \quad \sigma_{t,i}(z_t) = \frac{\phi_i(\hat{\mathbf{s}}_t) + \rho}{\sum_{j=1}^M (\phi_j(\hat{\mathbf{s}}_t) + \rho)} \quad (24)$$

where  $\rho > 0$  is the same baseline as in the offline stage, ensuring a well-defined coordinate during nominal operation (all  $\delta_i = 0$ ), and a first-order low-pass filter suppresses chattering when any  $\delta_i$  hovers near an

activation threshold. The exponential structure of  $\phi_i$  produces a smooth, physics-driven priority shift: under nominal operation where all  $\delta_i$  are small, the slow performance component of  $\sigma_t$  dominates; as any  $\delta_i \rightarrow 1$ , the explosive growth of the corresponding  $\phi_i$  drives  $\sigma_{t,i} \rightarrow 1$  continuously, redirecting the flow toward constraint restoration without any threshold or rule-based switching. This is the online counterpart of the offline semantic labeling of Section 3.2: the same potential that shaped the manifold geometry during training now shapes the navigation direction at runtime.

**Timescale separation from a single energy.** The scalar  $\epsilon > 0$  in (20) encodes the ratio between the fast and slow timescales of the control problem:

$$\epsilon = \frac{T_{\text{fast}}}{T_{\text{slow}}} \quad (25)$$

with  $T_{\text{fast}}$  the required constraint-restoration time and  $T_{\text{slow}}$  the performance-optimization horizon. Because  $1/\epsilon \gg 1$ , the normal potential is a steep well orthogonal to  $\mathcal{M}^*$ , while the tangential potential is a shallow landscape along it. Descending  $V$  therefore produces two regimes from the same gradient:

- **Snap** ( $O(\epsilon)$ , off-manifold):  $(1/\epsilon)\nabla_z \Phi_{\text{normal}}$  dominates and rapidly restores  $z_t$  to  $\mathcal{M}^*$  before any significant tangential motion occurs.
- **Slide** ( $O(1)$ , on-manifold):  $\Phi_{\text{normal}} \approx 0$  and  $\nabla_z \Phi_{\text{tangent}}$  navigates along  $\mathcal{M}^*$  toward the state satisfying the current priority  $\sigma_t(z_t)$ .

The two regimes are not implemented; they emerge. No explicit switching condition, no controller handoff, and no timescale-specific tuning is required.

**Remark 8** (Extension to  $K$  Timescales). *Systems with  $K$  well-separated timescales are accommodated by  $K - 1$  nested singular perturbation levels:*

$$V(z_t, \mathbf{x}_t) = \sum_{k=1}^{K-1} \frac{1}{\epsilon^k} \Phi_k(z_t, \mathbf{x}_t) + \Phi_K(z_t)$$

with  $1/\epsilon^{K-1} \gg \dots \gg 1/\epsilon \gg 1$  enforcing strict priority across levels. The present formulation retains  $K = 2$ , which is sufficient for the applications considered below.

### 4.3 Geometry-Aware State Evolution

Given the nominal field  $\mathbf{F}(z_t, \mathbf{x}_t)$ , the latent state is advanced by a single geometry-aware integrator that combines a second-order Runge-Kutta predictor, a curvature-aware residual computed in a decoder-induced metric basis, an optional retraction onto  $\mathcal{M}^*$ , and a final output clamp on the decoded action. The integrator is deterministic and non-iterative.

The nominal field is evaluated at a midpoint following a standard second-order Runge-Kutta scheme (Appendix A); the resulting Euclidean step  $\Delta z_{\text{Euc}}$  is then corrected as follows.

**Lie-local residual correction.** The Euclidean predictor treats all latent directions uniformly, ignoring the fact that the decoder  $D_s$  induces a non-trivial Riemannian metric on  $\mathcal{Z}$ . We correct this with a small geometry-aware residual computed in a local metric basis. The decoder-pullback metric at  $z_t$  is:

$$G(z_t) = J_{D_s}(z_t)^\top J_{D_s}(z_t) + \lambda_m \mathbf{I} \quad (26)$$

whose eigendecomposition yields principal directions of decoder sensitivity. Retaining the top- $k$  eigenvectors  $B \in \mathbb{R}^{n_z \times k}$  (typically  $k = 3$ ) and their scales  $\mathbf{s} = \sqrt{\text{diag}(\Lambda_{[-k:]})}$  identifies the directions along which latent motion produces the largest first-order change in the decoded state. Projecting the Euclidean step into this basis, partitioning into three-dimensional sub-blocks, and rotating each sub-block via an  $\mathfrak{so}(3)$  matrix exponential gives a curvature-aware residual:

$$\Delta z_{\text{Lie}} = B [\text{Rot}_{\mathfrak{so}(3)}(B^\top \Delta z_{\text{Euc}}, (B^\top k_2) \oslash \mathbf{s}; s_L, \Delta t) - B^\top \Delta z_{\text{Euc}}] \quad (27)$$

where  $\oslash$  is elementwise division (yielding scale-invariant angular velocities),  $s_L$  is a Lie-scale parameter, and sub-blocks of size less than two are left unrotated. The residual is deliberately small and guarded: it is confined to the top- $k$  eigendirections of  $G(z_t)$  and added to (rather than replacing) the Euclidean step, and a NaN-safe fallback  $\Delta z_{\text{Lie}} \leftarrow \mathbf{0}$  applies whenever any component is non-finite. This design ensures the correction acts only where the decoder geometry is informative, while the RK2 step continues to drive the bulk of the latent motion.

**Lie group integration and retraction.** The combined update is applied via left translation on the Lie group  $G$ , which preserves manifold membership algebraically by the closure axiom, followed by an optional retraction onto  $\mathcal{M}^*$ :

$$z_{t+1} = (1 - \mu_R) \bar{z}_{t+1} + \mu_R \Pi_{\mathcal{M}^*}(\bar{z}_{t+1}), \quad \bar{z}_{t+1} \triangleq z_t \oplus (\Delta z_{\text{Euc}} + \gamma_L \Delta z_{\text{Lie}}) \quad (28)$$

Here  $\gamma_L \in [0, 1]$  controls the strength of the Lie residual and  $\mu_R \in [0, 1]$  controls the retraction mix. Setting  $\gamma_L = \mu_R = 0$  recovers pure RK2; small  $\gamma_L \in [0.05, 0.2]$  adds curvature awareness without destabilizing the primary dynamics;  $\mu_R > 0$  suppresses any residual off-manifold drift. The next control action is decoded and clamped to its physical box bounds:

$$\mathbf{u}_{t+1} = \text{clip}(D_u(z_{t+1}), \mathbf{u}^{\min}, \mathbf{u}^{\max}) \quad (29)$$

which provides a hard, model-independent guarantee for box constraints.

**Remark 9** (Feasibility of the Decoded Action). *Because every training sample is generated by solving the multi-objective problem to feasibility, all points on  $\mathcal{M}^*$  decode to feasible actions. Combined with the Lipschitz continuity of  $D_u$  and the velocity cap  $V_{\max} \Delta t \leq \delta_{\text{feas}}$ , this guarantees  $\mathbf{f}(\mathbf{u}_t) \leq \mathbf{0}$  at every cycle without runtime constraint solving. See Proposition 2 in the appendix for the formal statement and proof, which covers both convex and nonconvex objectives.*

**Remark 10** (Additions Fit Within Proposition 1). *The velocity cap enforces  $\|\dot{z}\| \leq V_{\max}$  directly; the Lie residual is bounded by  $\|\gamma_L \Delta z_{\text{Lie}}\| \leq \gamma_L \Delta t V_{\max}$  by construction; the retraction is a non-expansion on  $\mathcal{M}^*$ . All three additions fit within the drift bound of Proposition 1 without modifying the non-accumulation argument, and the end-to-end action error bound of Theorem 1 remains valid.*

#### 4.4 Online Algorithm

---

##### Algorithm 1 Online Pareto Map Navigation

---

**Require:**  $\mathbf{x}_t, z_{t-1}, \hat{\sigma}_t^2, \tau_{\text{geom}}, \Delta t, \alpha, \epsilon, V_{\max}, \lambda_m, (k, \gamma_L, s_L), \mu_R, (\mathbf{u}^{\min}, \mathbf{u}^{\max})$   
**Ensure:**  $\mathbf{u}_{t+1}, z_{t+1}$   
**// 1: Manifold Localization**  
 $z_{\text{obs},t} \leftarrow E_x(\mathbf{x}_t); \quad \mathcal{M}_t \leftarrow \{z \in \mathcal{M}^* \mid \|\mathbf{x}_t - D_s(z)\|^2 \leq \hat{\sigma}_t^2 + \tau_{\text{geom}}\}$   
 $z_t \leftarrow (1 - \alpha) z_{t-1} + \alpha \arg \min_{z \in \mathcal{M}_t} \|z - z_{\text{obs},t}\|^2$   
**// 2: Energy Function & Nominal Field** *// single autograd pass*  
 $\hat{\mathbf{s}}_t \leftarrow D_s(z_t); \quad \sigma_{t,i} \leftarrow (\phi_i + \rho) / \sum_j (\phi_j + \rho)$  (eq. (9));  $\mathbf{F}(z_t) \leftarrow -\nabla_z \left[ \frac{1}{\epsilon} \|\mathbf{x}_t - D_s(z_t)\|^2 + \sum_i \sigma_{t,i} J_i(D_s, D_u) \right]$   
**// 3: RK2 Predictor** *// cap each slope at  $V_{\max}$*   
Compute  $k_1, z_{\text{mid}}, k_2, \Delta z_{\text{Euc}}$  via RK2 (App. A) with  $\Pi_{\|\cdot\| \leq V_{\max}}$   
**// 4: Lie-Local Residual Correction**  
 $G \leftarrow J_{D_s}^\top J_{D_s} + \lambda_m \mathbf{I}; \quad (B, \mathbf{s}) \leftarrow \text{top-}k \text{ eigenbasis of } G$   
 $\Delta z_{\text{Lie}} \leftarrow B [\text{Rot}(B^\top \Delta z_{\text{Euc}}, (B^\top k_2) \oslash \mathbf{s}; s_L, \Delta t) - B^\top \Delta z_{\text{Euc}}]$  *// NaN  $\rightarrow \mathbf{0}$*   
**// 5: Lie Group Integration, Retraction & Decode**  
 $\bar{z}_{t+1} \leftarrow z_t \oplus (\Delta z_{\text{Euc}} + \gamma_L \Delta z_{\text{Lie}}); \quad z_{t+1} \leftarrow (1 - \mu_R) \bar{z}_{t+1} + \mu_R \Pi_{\mathcal{M}^*}(\bar{z}_{t+1})$   
 $\mathbf{u}_{t+1} \leftarrow \text{clip}(D_u(z_{t+1}), \mathbf{u}^{\min}, \mathbf{u}^{\max}); \quad \text{return } \mathbf{u}_{t+1}, z_{t+1}$

---

Algorithm 1 summarizes the complete online navigation cycle. Each iteration proceeds through five sequential steps: manifold localization from the partial observation, energy-function evaluation with a single shared

autograd pass yielding the nominal field  $\mathbf{F}(z_t)$ , an RK2 predictor with radial velocity cap, a Lie-local residual correction computed in the top- $k$  eigendirections of the decoder-pullback metric, and Lie group integration with optional retraction and output clamping. The entire cycle is deterministic and non-iterative in its outer loop: two autograd passes (for  $k_1$  and  $k_2$ ) and one small  $k \times k$  eigendecomposition (typically  $k \leq 3$ ) together constitute the dominant computational cost, all executing in milliseconds for systems of practical scale. No online learning, parameter update, or iterative solver is invoked. All numerically sensitive operations are guarded by NaN-safe fallbacks, the geometric drift introduced by Lie group integration is provably non-accumulating by Proposition 1 (asymptotic) and Proposition 3 (uniform, closed-loop), and feasibility of the decoded action follows from Remark 9 and Proposition 2, ensuring long-horizon stability without any additional correction mechanism.

## 5 Analytical Benchmarks and OPF Instantiation

### 5.1 Analytical Dynamic Navigation with Convex Objectives

Before instantiating GPC on the full multi-objective optimal power flow problem of Section 5.3, we define analytical navigation benchmarks where the Pareto manifold, semantic coordinate evolution, and latent trajectories can be visualized directly. These controlled settings isolate the mechanisms of Algorithm 1; the corresponding simulation results and ablations are reported in Section 6.

**Problem setup.** We use a constrained dynamic navigation problem that has the same structure as a standard safe-RL benchmark but remains analytically visualizable. The physical state is  $\mathbf{s}_t = (\mathbf{q}_t, \mathbf{v}_t) \in \mathbb{R}^4$ , where  $\mathbf{q}_t \in \mathbb{R}^2$  is position and  $\mathbf{v}_t \in \mathbb{R}^2$  is velocity. The control action  $\mathbf{u}_t \in \mathbb{R}^2$  is acceleration, and the system obeys double-integrator dynamics:

$$\mathbf{q}_{t+1} = \mathbf{q}_t + \Delta t \mathbf{v}_t + \frac{1}{2} \Delta t^2 \mathbf{u}_t, \quad (30)$$

$$\mathbf{v}_{t+1} = \mathbf{v}_t + \Delta t \mathbf{u}_t. \quad (31)$$

Thus the current decision cannot instantaneously choose a point on the Pareto front; it must act through the system dynamics, as in an RL control environment.

The two objectives are evaluated on the dynamically propagated next state:

$$J_1(\mathbf{s}_t, \mathbf{u}_t, p_t) = \|\mathbf{q}_{t+1} - \mathbf{q}_{\text{safe}}(p_t)\|^2, \quad (32)$$

$$J_2(\mathbf{s}_t, \mathbf{u}_t) = \|\mathbf{q}_{t+1} - \mathbf{q}_{\text{goal}}\|^2 + \beta_u \|\mathbf{u}_t\|^2. \quad (33)$$

Here  $J_1$  is the safety objective, pulling the system toward a load-dependent recovery location  $\mathbf{q}_{\text{safe}}(p_t)$ , while  $J_2$  is the performance objective, pulling the system toward the mission goal with small control effort.

The scalar operating condition  $p_t$  shifts a moving elliptical keep-out region, analogous to a load-driven security boundary in OPF. Let  $\mathbf{c}(p_t) = \mathbf{c}_0 + \rho p_t$  be its center. The nonconvex state constraint requires the next position to remain outside the ellipse:

$$g_{\text{obs}}(\mathbf{q}_{t+1}, p_t) = 1 - \frac{(q_{1,t+1} - c_1(p_t))^2}{a^2} - \frac{(q_{2,t+1} - c_2(p_t))^2}{b^2} \leq 0. \quad (34)$$

The dynamic constraints are the input bound and a ramp-rate-like slew constraint:

$$\|\mathbf{u}_t\| \leq u_{\text{max}}, \quad \|\mathbf{u}_t - \mathbf{u}_{t-1}\| \leq r_{\text{max}}. \quad (35)$$

The moving obstacle creates a curved, nonconvex, time-varying feasible region, while the slew constraint introduces temporal coupling between consecutive actions. This is the essential dynamic constraint structure that model-free constrained RL can represent, but GPC solves by navigating the precomputed Pareto manifold rather than by learning a policy through rollout.

For each context  $\xi_t = (\mathbf{s}_t, \mathbf{u}_{t-1}, p_t)$ , the dynamically feasible Pareto set is obtained by sweeping  $\mathbf{w} \in \Delta^1$  in:

$$\mathbf{u}^*(\mathbf{w}; \xi_t) = \arg \min_{\mathbf{u}_t} w_1 J_1(\mathbf{s}_t, \mathbf{u}_t, p_t) + w_2 J_2(\mathbf{s}_t, \mathbf{u}_t) \quad \text{s.t.} \quad (31) - (35). \quad (36)$$

These solutions define a low-dimensional Pareto manifold  $\mathcal{M}^*$  over dynamic operating contexts rather than a static curve in action space. During nominal operation,  $\boldsymbol{\sigma}_t$  is performance dominated and GPC slides along the dynamically feasible arc toward  $\mathbf{q}_{\text{goal}}$ . During a constraint event, the moving ellipse intersects the predicted trajectory; the normal potential first snaps the latent state back to the dynamically feasible manifold, and the tangential potential then slides along the manifold toward the safety-dominated region. A fixed-weight baseline is trapped by its constant scalarization and either reacts late or violates the obstacle or slew constraint.

## 5.2 Analytical Dynamic Navigation with Nonconvex Objective

The convex-objective benchmark above tests dynamic constraints and semantic priority adaptation while keeping the scalarized objective landscape simple. To test navigation over a nonconvex objective landscape, we keep the same double-integrator dynamics, moving obstacle, input bound, and slew constraint, but replace the performance objective by a smooth multi-basin objective:

$$J_2^{\text{nc}}(\mathbf{s}_t, \mathbf{u}_t) = \|\mathbf{q}_{t+1} - \mathbf{q}_{\text{goal}}\|^2 + \beta_u \|\mathbf{u}_t\|^2 + \lambda_{\text{nc}} \sum_{\ell=1}^2 [1 - \cos(\omega(q_{\ell,t+1} - q_{\text{goal},\ell}))]. \quad (37)$$

The sinusoidal term introduces local basins around the nominal goal while preserving differentiability. The corresponding Pareto set is:

$$\mathbf{u}_{\text{nc}}^*(\mathbf{w}; \xi_t) = \arg \min_{\mathbf{u}_t} w_1 J_1(\mathbf{s}_t, \mathbf{u}_t, p_t) + w_2 J_2^{\text{nc}}(\mathbf{s}_t, \mathbf{u}_t) \quad \text{s.t.} \quad (31) - (35). \quad (38)$$

This benchmark is still low-dimensional enough to visualize, but it requires the learned Pareto map to encode a genuinely nonconvex trade-off surface. In a constrained RL formulation the same problem can be represented by a reward and safety cost; in GPC the nonconvex Pareto family is solved offline and then traversed online by the same geometric navigator.

## 5.3 Multi-Objective Optimal Power Flow Control with Multi-Timescale Dynamics

To make the GPC framework concrete, we instantiate it on multi-objective AC optimal power flow. The framework is not specific to power systems: any application where the governing physics is known and the control problem takes the form of (39) is directly supported. Wireless resource allocation, for instance, maps naturally to this structure with interference coupling equations replacing the AC power flow equalities and rate-quality constraints replacing thermal limits Luong et al. (2019); Feriani & Hossain (2021). Transportation network control involves polynomial flow conservation equations on sparse graphs with capacity and ramp-rate constraints of identical mathematical form Haydari & Yilmaz (2020); Zong et al. (2025). Building energy management, water distribution, and chemical process control all share the same three-block structure of nonlinear equalities, inequality safety constraints, and temporal coupling.

AC-OPF is chosen as the primary instantiation precisely because it is among the hardest instances of this class: the feasibility set  $\mathbf{g}(\mathbf{s}, \mathbf{u}) = \mathbf{0}$  is dense, non-separable, and nonconvex due to trigonometric voltage phasor interactions, and the three objectives span timescales differing by four orders of magnitude. A method that succeeds on AC-OPF therefore provides the strongest available evidence of deployability across the full CPS spectrum. For readers unfamiliar with power systems, the problem takes the following general mathematical form. Given a network of  $n_{\text{bus}}$  nodes and  $n_{\text{gen}}$  controllable inputs, find  $\mathbf{u} \in \mathbb{R}^{n_u}$  solving:

$$\min_{\mathbf{u}} \quad \mathbf{w}^\top \mathbf{J}(\mathbf{s}, \mathbf{u}) \quad \text{subject to} \quad \begin{cases} \mathbf{g}(\mathbf{s}, \mathbf{u}) = \mathbf{0} & \text{(nonlinear equality)} \\ \mathbf{f}(\mathbf{s}, \mathbf{u}) \leq \mathbf{0} & \text{(inequality constraints)} \\ \mathbf{c}(\mathbf{u}_t, \mathbf{u}_{t-1}) \leq \mathbf{0} & \text{(temporal coupling)} \end{cases} \quad (39)$$

where  $g$  is a set of dense, coupled nonlinear equalities (the AC power flow equations) that define the feasibility manifold in state space,  $\mathbf{f}$  collects box and network safety constraints, and  $\mathbf{c}$  encodes inter-step temporal coupling. The objective vector  $\mathbf{J} \in \mathbb{R}^3$  has three components ordered by timescale and safety priority:  $J_1$  (safety-critical, seconds),  $J_2$  (quality-of-service, minutes), and  $J_3$  (economic, tens of minutes to hours). The

weight vector  $\mathbf{w} \in \Delta^2$  is not fixed; it must be computed autonomously from real-time observations, which is precisely the role of the semantic coordinate  $\boldsymbol{\sigma}_t$  derived in Section 3.

Problem (39) must be solved repeatedly at every dispatch interval  $\Delta t$  under continuously varying exogenous disturbance  $\mathbf{p}_t$ , with a hard real-time deadline that precludes iterative solvers for large networks. The remainder of this section specifies the concrete instantiation of each GPC component for this problem class.

### 5.3.1 System Model and Multi-Objective Formulation

Consider a transmission network with  $n_{\text{bus}}$  buses,  $n_{\text{gen}}$  generators, and branch set  $\mathcal{L}$ . Let  $V_i \in \mathbb{R}_{>0}$  and  $\theta_i \in \mathbb{R}$  denote the voltage magnitude and phase angle at bus  $i$ , and let  $Y_{\text{bus}} = G + jB \in \mathbb{C}^{n_{\text{bus}} \times n_{\text{bus}}}$  denote the network admittance matrix. The system state is the voltage phasor vector  $\mathbf{s}_t = [\mathbf{V}_t, \boldsymbol{\theta}_t] \in \mathbb{R}^{2n_{\text{bus}}}$ , the control action is the generator dispatch  $\mathbf{u}_t = [P_{\text{gen}}, Q_{\text{gen}}] \in \mathbb{R}^{2n_{\text{gen}}}$ , and the exogenous disturbance is the load demand  $\mathbf{p}_t = [P_{\text{load}}, Q_{\text{load}}]$ , which varies continuously and is not controllable. The partial observation available at deployment is:

$$\mathbf{x}_t = h(\mathbf{s}_t) + \boldsymbol{\eta}_t \in \mathbb{R}^{n_x} \quad (40)$$

where  $h$  extracts bus-level quantities  $(V_i, P_i, Q_i)$  at a monitored subset of buses via AMI infrastructure, with  $n_x \ll 2n_{\text{bus}}$ . The offline dataset takes the base form of Section 3:

$$\mathcal{D} = \{(\mathbf{x}_k, \mathbf{u}_k, \mathbf{s}_k, \boldsymbol{\sigma}_k, \mathbf{J}_k)\}_{k=1}^N \quad (41)$$

where  $\boldsymbol{\sigma}_k \in \Delta^2$  is the three-component semantic priority coordinate over thermal, voltage, and economic objectives, and  $\mathbf{J}_k = [J_1(\mathbf{s}_k, \mathbf{u}_k), J_2(\mathbf{s}_k, \mathbf{u}_k), J_3(\mathbf{u}_k)]^\top$  is the objective vector.

**AC power flow equations.** The physical state must satisfy the AC power balance equations at every bus  $i$ :

$$P_{\text{gen},i} - P_{\text{load},i} = V_i \sum_{j=1}^{n_{\text{bus}}} V_j [G_{ij} \cos(\theta_i - \theta_j) + B_{ij} \sin(\theta_i - \theta_j)] \quad (42)$$

$$Q_{\text{gen},i} - Q_{\text{load},i} = V_i \sum_{j=1}^{n_{\text{bus}}} V_j [G_{ij} \sin(\theta_i - \theta_j) - B_{ij} \cos(\theta_i - \theta_j)] \quad (43)$$

These nonlinear equality constraints define the AC feasibility manifold in state space. In GPC, they are not enforced explicitly at runtime; instead, every sample in  $\mathcal{D}$  is generated by solving the full AC-OPF to feasibility, so the power flow equations are embedded implicitly in the geometry of  $\mathcal{M}^*$ . At runtime, the state decoder  $D_s(z_t)$  reconstructs a power-flow-consistent state  $\hat{\mathbf{s}}_t = [\hat{\mathbf{V}}_t, \hat{\boldsymbol{\theta}}_t]$  directly from the latent state, and all violation indicators are evaluated on  $\hat{\mathbf{s}}_t$ .

**Branch flows.** The apparent power flow on branch  $(i, j)$  is  $S_{ij} = \sqrt{P_{ij}^2 + Q_{ij}^2}$ , where:

$$P_{ij} = V_i^2 G_{ij} - V_i V_j [G_{ij} \cos(\theta_i - \theta_j) + B_{ij} \sin(\theta_i - \theta_j)] \quad (44)$$

$$Q_{ij} = -V_i^2 B_{ij} - V_i V_j [G_{ij} \sin(\theta_i - \theta_j) - B_{ij} \cos(\theta_i - \theta_j)] \quad (45)$$

Branch flows are not directly observed by AMI infrastructure, which provides bus-level quantities  $(V_i, P_i, Q_i)$  at a subset of buses only. They are reconstructed from the decoded voltage phasors  $(\hat{V}_i, \hat{\theta}_i)$  extracted from  $\hat{\mathbf{s}}_t = D_s(z_t)$  via the known  $Y_{\text{bus}}$ , eliminating the need for a dedicated state estimator.

**Inequality constraints.** The feasible action set is further restricted by:

$$P_{\text{gen},i}^{\min} \leq P_{\text{gen},i} \leq P_{\text{gen},i}^{\max}, \quad Q_{\text{gen},i}^{\min} \leq Q_{\text{gen},i} \leq Q_{\text{gen},i}^{\max} \quad (\text{generator capacity}) \quad (46)$$

$$V_i^{\min} \leq V_i \leq V_i^{\max} \quad (\text{voltage limits}) \quad (47)$$

$$S_{ij} \leq S_{\text{max},ij} \quad (\text{branch thermal limits}) \quad (48)$$

$$|P_{\text{gen},i,t} - P_{\text{gen},i,t-1}| \leq \delta_{\text{ramp}} \quad (\text{ramp-rate limits}) \quad (49)$$

Ramp-rate limits couple consecutive dispatch decisions and constitute the primary source of multi-timescale complexity: they prevent the fast thermal objective from being satisfied instantaneously, requiring the navigator to plan a feasible trajectory across multiple steps. Inequality constraints are handled by the geometry encoded in  $\mathcal{M}^*$ , the output clamp for box constraints, and, when hard per-step coupling enforcement is enabled, a local Jacobian projection via the action Jacobian  $\mathbf{J}_t$ , with each active constraint type contributing rows to  $A_t$  and  $b_t$ .

**Three-objective hierarchy.** The MO-OPF instantiates the general objective vector  $\mathbf{J}(\mathbf{s}_t, \mathbf{u}_t)$  with three terms ordered by timescale and safety priority.

$J_1$  penalizes thermal overloading via a quartic potential that rises explosively as branch loading approaches the thermal rating:

$$J_1(\mathbf{s}_t) = \sum_{(i,j) \in \mathcal{L}} \left[ \max \left( 0, \frac{S_{ij}}{S_{ij}^{\max}} - \tau \right) \right]^4, \quad \tau = 0.85 \quad (50)$$

The quartic exponent and the  $\tau = 0.85$  margin create a steep potential wall that activates before the hard thermal limit is reached, consistent with the singular perturbation structure of the semantic potentials in Section 3.2.

$J_2$  penalizes voltage deviations outside an acceptable deadband around the nominal value of 1.0 p.u.:

$$J_2(\mathbf{s}_t) = \sum_{i=1}^{n_{\text{bus}}} \max(0, |V_i - 1.0| - \delta_{\text{dead}})^2, \quad \delta_{\text{dead}} = 0.05 \text{ p.u.} \quad (51)$$

The deadband avoids penalizing small deviations within the acceptable operating range, concentrating the gradient signal on genuine voltage quality violations.

$J_3$  models the economic cost of generation via the standard quadratic heat rate characteristic:

$$J_3(\mathbf{u}_t) = \sum_{i=1}^{n_{\text{gen}}} [a_i P_{\text{gen},i}^2 + b_i P_{\text{gen},i} + c_i] \quad (52)$$

where  $a_i, b_i, c_i$  are generator-specific cost coefficients determined from historical fuel cost data.

### 5.3.2 GPC Instantiation: Semantic Violation Indicators

The general violation indicators  $\delta_i(\hat{\mathbf{s}}_t) \in [0, 1]$  of Section 3.2 are instantiated on the reconstructed state  $\hat{\mathbf{s}}_t = D_s(z_t)$  as follows. The thermal indicator measures the worst-case branch loading across the network:

$$\delta_f(\hat{\mathbf{s}}_t) = \text{clip} \left( \max_{(i,j) \in \mathcal{L}} \frac{\hat{S}_{ij}}{S_{ij}^{\max}}, 0, 1 \right) \quad (53)$$

The voltage indicator measures the worst-case normalized deviation from nominal across all buses:

$$\delta_v(\hat{\mathbf{s}}_t) = \text{clip} \left( \frac{\max_i |\hat{V}_i - V_{\text{nom}}|}{\Delta V_{\text{limit}}}, 0, 1 \right) \quad (54)$$

The economic indicator  $\delta_e$  is set to a small positive constant  $\delta_e \ll 1$ , encoding a persistent background drive toward economic operation that remains active whenever thermal and voltage conditions are benign. Together, the three indicators  $(\delta_f, \delta_v, \delta_e)$  feed the autonomous semantic generation of Section 4.2 to produce the urgency potentials:

$$\phi_i(\hat{\mathbf{s}}_t) = \exp \left( \frac{k_i \cdot \delta_i(\hat{\mathbf{s}}_t)}{\epsilon_i} \right) - 1 \quad (55)$$

and the semantic priority coordinate  $\sigma_{t,i} = (\phi_i(\hat{\mathbf{s}}_t) + \rho) / \sum_j (\phi_j(\hat{\mathbf{s}}_t) + \rho) \in \Delta^2$  (equation (9)), which shifts continuously from  $\sigma_{t,3} \approx 1$  (economic dominance) to  $\sigma_{t,1} \approx 1$  (thermal emergency) without any rule-based switching.

## 6 Experimental Validation

### 6.1 Experimental Setup

We evaluate GPC on two simulation groups: analytical dynamic navigation and IEEE 30-bus OPF. The analytical simulations include both the convex-objective benchmark of Section 5.1 and the nonconvex-objective benchmark of Section 5.2. These cases isolate the geometry and integration mechanisms in a fully visualizable setting. The OPF case tests the same mechanisms on the standard MATPOWER 30-bus network under thermal/voltage/economic objectives. We additionally run the training-time system uncertainty simulations of Section 6.4; these stress tests perturb the physical parameters of the same network rather than introducing additional larger-network cases.

All ground-truth AC-OPF solutions are generated via IPOPT through MATPOWER with convergence tolerance  $10^{-6}$ . For the IEEE 30-bus case, the offline dataset  $\mathcal{D}$  is constructed via Latin Hypercube Sampling with  $N = 5000$  load scenarios, each solved for  $|\mathcal{W}| = 50$  uniformly spaced weight vectors across  $\Delta^2$ , yielding 250,000 certified Pareto-optimal samples. Load profiles span  $[0.6, 1.4]$  times the nominal MATPOWER loading.

For the uncertainty-aware training (Case 3), the physical parameter vector  $\theta$  is sampled jointly with load and objective weights during offline data generation. Case 3 restricts perturbations to branch admittances only ( $\xi^S = \xi^c = 0$ ):

$$Y_{ij}(\theta) = Y_{ij}^0(1 + \xi_{ij}^Y), \quad \xi_{ij}^Y \in [-\rho_Y, \rho_Y], \quad (56)$$

with  $(\sigma_Y, \rho_Y) = (0.01, 0.03)$ . Each trajectory samples a single admittance realization held fixed for all  $H + 1$  dispatch steps, reflecting the physical timescale separation between line-parameter drift (hours) and OPF dispatch (seconds). The sampled  $\theta$  is appended to the physical input  $\mathbf{x}_k$  so the offline map learns a family of Pareto manifolds indexed by uncertain network realizations.

The encoders  $E_x, E_s$  and decoders  $D_u, D_s$  are three-layer MLPs with hidden dimension 256, ReLU activations, and spectral normalization, trained for 500 epochs with Adam (lr =  $10^{-3}$ , cosine annealing), loss weights  $\omega_1 = 1.0, \omega_2 = 0.5$ , and neighborhood size  $\kappa = 10$ . The latent dimension is  $n_z = 32$  for the 30-bus OPF cases. Online navigation uses  $\epsilon = 0.05, \alpha = 0.3$ , and  $\tau_{\text{geom}}$  calibrated to  $\mathcal{L}_{\text{local}}^{\text{val}}$ , running at  $\Delta t = 5$  seconds on a single CPU core.

We compare GPC against three baselines throughout all cases. **TD3** Fujimoto et al. (2018) is a model-free deep RL agent trained on the nominal environment and transferred zero-shot. **CPO** Achiam et al. (2017) is a constrained policy optimization method trained with the same constraint specification. **MPC** is a receding-horizon controller that solves a linearised version of the problem online at each dispatch step using the current system state. For the analytical cases (Case 1) we additionally compare against **Online scalarization**, which solves the scalarized objective at each step via the teacher oracle, and evaluate against a finite-horizon dynamic-programming (DP) oracle. For the OPF cases (Cases 2 and 3) the optimality reference is the full **MO-IPOPT** Pareto solver and the single-objective **runopf** economic dispatch, both run offline. All RL baselines are trained for  $10^6$  environment interactions. Performance is reported as feasibility rate, suboptimality relative to the oracle, and mean wall-clock decision latency.

Table 1: Simulation cases.

Case	System	Constraints	Purpose
Case 1: Analytical	2D double integrator	Obstacle, input, slew	Mechanism visualization
Case 2: Nominal OPF	IEEE 30-bus	Thermal, voltage, ramp	OPF baseline comparison
Case 3: Uncertain OPF	IEEE 30-bus	Same + branch admittance noise	Robustness to network uncertainty

Table 2: Analytical dynamic navigation: optimality and feasibility comparison ( $n = 100$  trajectories).  $R_T$  reported as mean  $\pm$  s.e.m. (%).  $\dagger$ : non-zero failure rate (rollout terminated early). Lower  $R_T$ , fewer violations, lower Fail, and lower runtime are better. Best non-oracle result in **bold**.

Obj.	Method	$R_T$ (%)	Obs. viol. (%)	Slew viol. (%)	Fail (%)	Time (ms)
Convex	Oracle	0.00	0.0	0.0	0	offline
Convex	TD3 $\dagger$	8.95 $\pm$ 0.40	0.08	52.5	99	0.11
Convex	CPO	382.5 $\pm$ 9.91	0.0	0.0	0	0.10
Convex	MPC	9.93 $\pm$ 0.51	0.0	0.0	0	1025
Convex	Online $\dagger$	7.90 $\pm$ 0.35	0.0	0.0	67	0.03
Convex	<b>GPC<math>\dagger</math></b>	<b>0.043 <math>\pm</math> 0.011</b>	<b>0.0</b>	<b>0.0</b>	0	0.78
Nonconvex	Oracle	0.00	0.0	0.0	0	offline
Nonconvex	TD3 $\dagger$	15.11 $\pm$ 0.68	0.07	75.6	100	0.21
Nonconvex	CPO	370.6 $\pm$ 9.59	0.0	0.0	0	0.24
Nonconvex	MPC	9.43 $\pm$ 0.52	0.0	0.0	0	1230
Nonconvex	Online $\dagger$	7.90 $\pm$ 0.38	0.0	0.0	79	14.65
Nonconvex	<b>GPC<math>\dagger</math></b>	<b>0.050 <math>\pm</math> 0.011</b>	<b>0.0</b>	<b>0.0</b>	0	0.97

## 6.2 Case 1: Analytical Dynamic Navigation

The analytical simulations use the double-integrator system and moving obstacle of Sections 5.1 and 5.2. We evaluate the ability of GPC to trace the dynamically feasible Pareto front, recover from off-manifold perturbations, and shift  $\sigma_t$  from performance to safety when the obstacle intersects the predicted trajectory. The nonconvex variant tests whether the same latent navigator remains stable when the objective landscape contains multiple local basins.

Because this benchmark is low-dimensional, we can compute an explicit finite-horizon dynamic-programming (DP) oracle by discretizing  $(\mathbf{q}, \mathbf{v}, \mathbf{u})$  and solving the constrained Bellman recursion with the same moving obstacle, input bound, and slew constraint. DP is used only as an evaluation oracle; it is not available for the higher-dimensional OPF cases. We compare GPC against this oracle and four baselines: **TD3** Fujimoto et al. (2018), a model-free deep RL agent; **CPO** Achiam et al. (2017), a constrained policy optimization method; **MPC**, a receding-horizon model predictive controller with the same physics model; and **Online scalarization**, which solves the scalarized objective at each step via the teacher oracle. The primary optimality metric is the normalized dynamic regret

$$R_t = \frac{\sum_{\tau=1}^t \sigma_\tau^\top (\mathbf{J}(\mathbf{s}_\tau, \mathbf{u}_\tau) - \mathbf{J}^{\text{DP}}(\mathbf{s}_\tau))}{\sum_{\tau=1}^t \sigma_\tau^\top \mathbf{J}^{\text{DP}}(\mathbf{s}_\tau) + \delta_R}, \quad (57)$$

where  $\delta_R > 0$  prevents division by zero. This curve directly tests whether the geometric navigator remains close to the trajectory-level constrained optimum, not merely whether it stays on the learned manifold.

Figures 2 and 3 report results for the convex- and nonconvex-objective variants, respectively. Each figure is organized around four panels. Panel (a) shows the terminal regret  $R_T$  of every method relative to the adaptive oracle on a log scale; hatched bars indicate runs that terminated early due to a constraint violation or solver infeasibility. Panel (b) shows the autonomous evolution of the semantic coordinate  $\sigma_t$  over the rollout: GPC adapts its safety/goal priority continuously, while fixed-weight baselines hold a constant scalarization. Panel (c) shows the closed-loop state-space trajectory; the red marker indicates the tightest obstacle-constraint step, and dashed curves indicate invalid or incomplete rollouts. Panel (d) plots terminal regret against mean per-step decision time on a log-log scale, revealing the speed-quality frontier; open markers denote failed or constraint-invalid runs.

Table 2 summarizes the same comparison quantitatively over  $n = 100$  independent trajectories.  $R_T$  is the normalized optimality gap relative to the adaptive oracle (eq. (57)), reported as mean  $\pm$  s.e.m. (%). Obstacle and slew violation columns give the percentage of rollout steps violating eq. (34) and eq. (35), respectively. Fail (%) is the fraction of trajectories that terminated before completing the full rollout due to a constraint

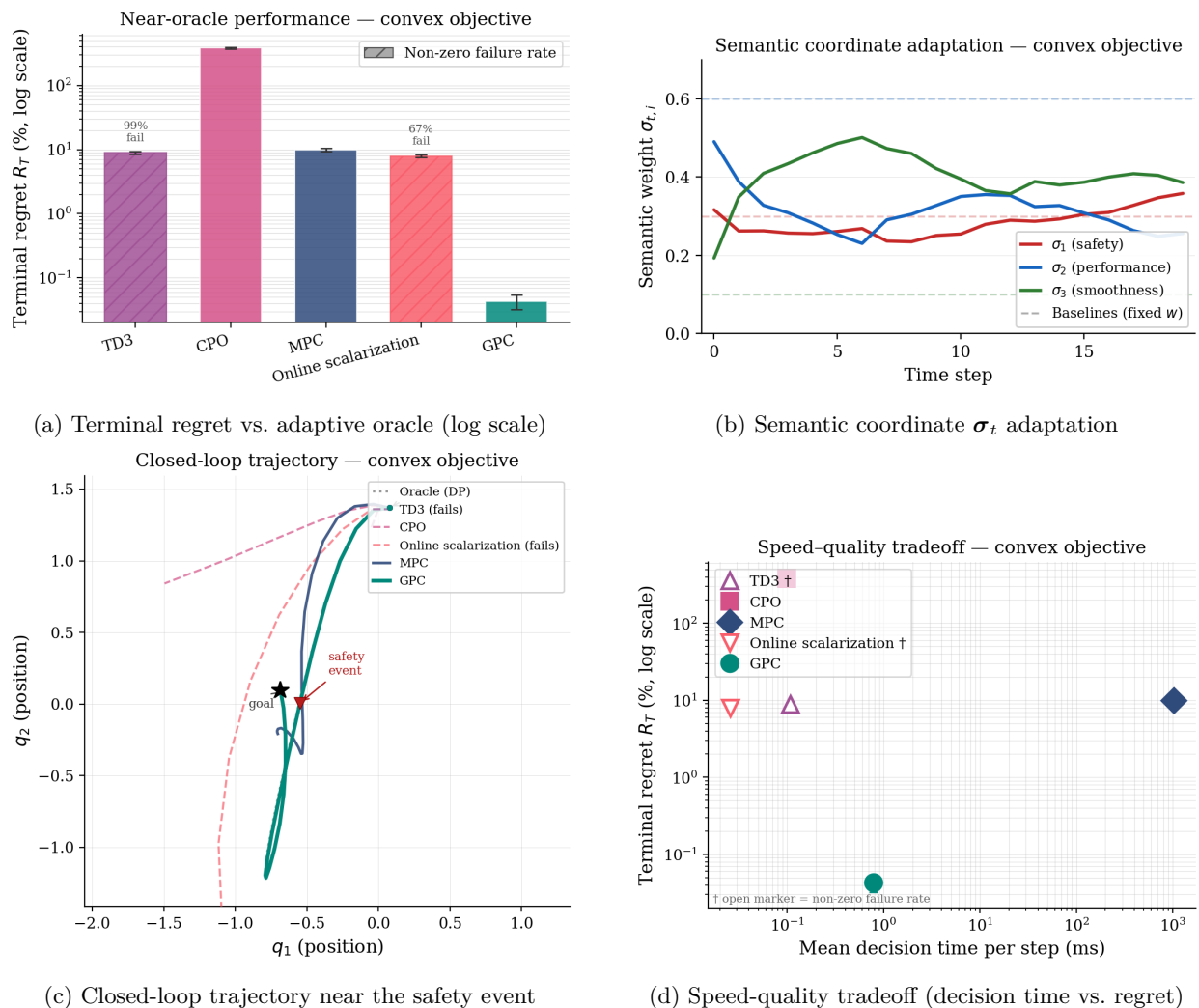


Figure 2: Analytical dynamic navigation: **convex objective** ( $n = 100$  independent trajectories). GPC achieves a mean terminal regret of 0.043%, two orders of magnitude below the next-best compliant baseline (MPC: 9.93%). TD3 fails in 99% of trajectories due to slow constraint violations (52.5% per-step violation rate); Online scalarization fails in 67% of trajectories due to solver infeasibility; CPO completes all trajectories but incurs mean regret of 382.5%. The semantic coordinate  $\sigma_t$  (panel b) shifts autonomously in response to the safety event, whereas fixed-weight baselines hold a constant scalarization throughout. GPC’s mean decision time of 0.78 ms is three orders of magnitude faster than MPC (1025 ms) at lower regret (panel d).

violation or solver infeasibility; methods with non-zero failure rate are marked †. The adaptive oracle has zero regret by definition and is included as an offline reference only. Reporting convex and nonconvex objective variants side by side makes clear that GPC’s advantage does not depend on convexity of the objective landscape.

### 6.3 Case 2: IEEE 30-Bus OPF

We evaluate GPC on 300-step load trajectories at  $\Delta t = 5$  s dispatch intervals on the nominal (no admittance perturbation) IEEE 30-bus network. Load profiles are drawn from a held-out test partition with no overlap with training data. We compare against MPC, TD3, and CPO, and evaluate tracking quality against the MO-IPOPT Pareto oracle and the single-objective `runopf` economic dispatch.

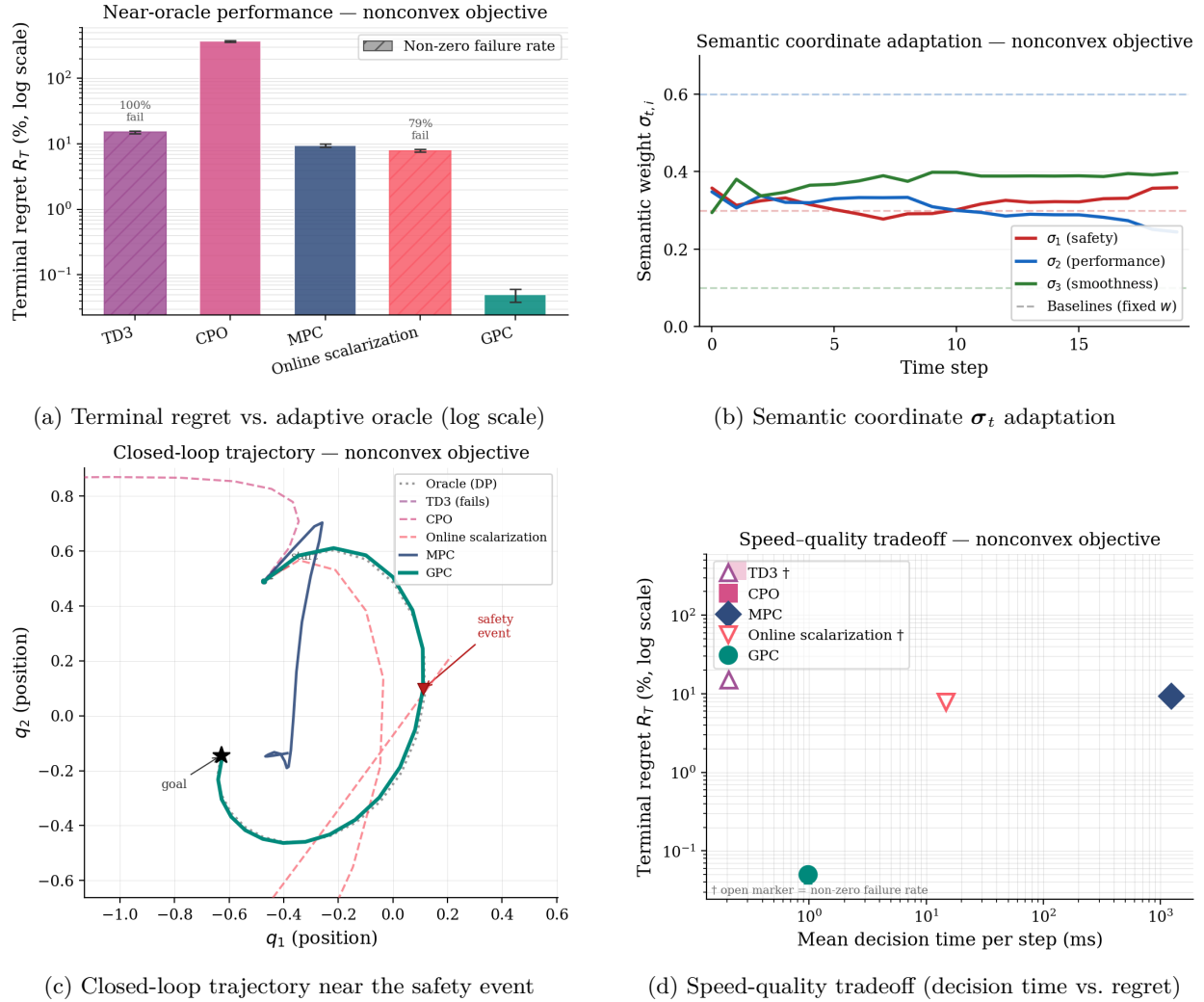
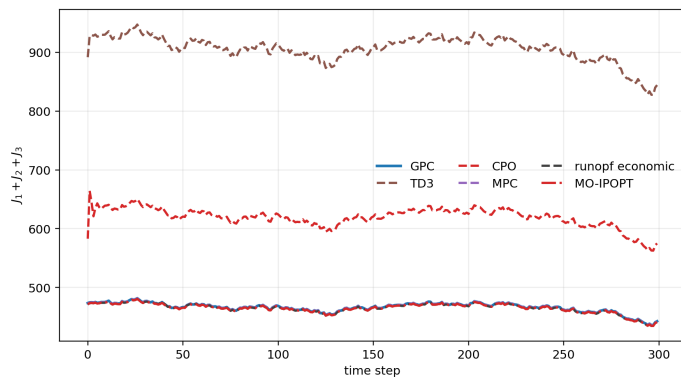


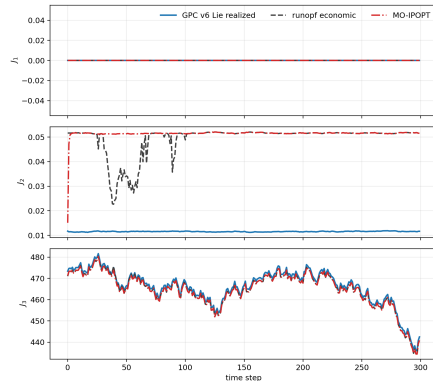
Figure 3: Analytical dynamic navigation: **nonconvex objective** ( $n = 100$  independent trajectories). The sinusoidal multi-basin structure does not degrade GPC’s performance: mean terminal regret of 0.050%, two orders of magnitude below the next-best compliant baseline (MPC: 9.43%). TD3 fails in all 100 trajectories (slew violation rate 75.6%); Online scalarization fails in 79% of trajectories. MPC is the strongest completing baseline but requires 1230 ms per decision step, rendering it unsuitable for real-time deployment. GPC maintains 0.97 ms per step while tracking the nonconvex Pareto front and adapting  $\sigma_t$  without mode switching (panel b).

Table 3: IEEE 30-bus nominal OPF (300 steps).  $\bar{\Delta}$ : mean per-step gap to MO-IPOPT oracle. **Bold**: best non-oracle.

Method	Mean $J_{\text{total}} \downarrow$	Feasible (%) $\uparrow$	Subopt. (%) $\downarrow$	Latency (ms)
MO-IPOPT oracle	360.00	100.0	0.00	$\gg 10^3$
runopf oracle	360.03	100.0	0.01	$\gg 10^3$
<b>GPC (ours)</b>	<b>361.08</b>	<b>100.0</b>	<b>0.30</b>	<b>12.3</b>
MPC	360.99	100.0	0.28	1193.8
CPO	519.78	0.0	44.4	0.19
TD3	743.77	0.0	106.6	0.17



(a)  $J_{\text{total}}$  vs. oracles over 300 steps.



(b) Individual objectives  $J_1$ ,  $J_2$ ,  $J_3$  vs. both oracles.

Figure 4: Case 2: IEEE 30-bus nominal OPF (300 steps). GPC and MPC track the oracle; model-free baselines fail entirely. GPC satisfies all three objective channels simultaneously with 0.30% suboptimality.

GPC achieves 100% feasibility and tracks the MO-IPOPT oracle to within 0.30% suboptimality ( $\bar{\Delta} = 1.08$  per step), virtually identical to MPC (0.28%) while running at  $97.1\times$  lower latency (12.3 ms vs. 1193.8 ms). Figure 4b shows that GPC simultaneously maintains  $J_1 \approx 0$  (thermal constraints satisfied), suppresses the voltage objective  $J_2$ , and tracks the economic oracle in  $J_3$ , with all three channels matched without mode switching. The oracle gap stabilises at  $\approx 1.08$  from step 50 onward and does not grow with the horizon, consistent with the non-accumulation guarantee of Theorem 1. TD3 and CPO produce zero feasible dispatches, with mean  $J_{\text{total}}$  44% and 107% above GPC respectively.

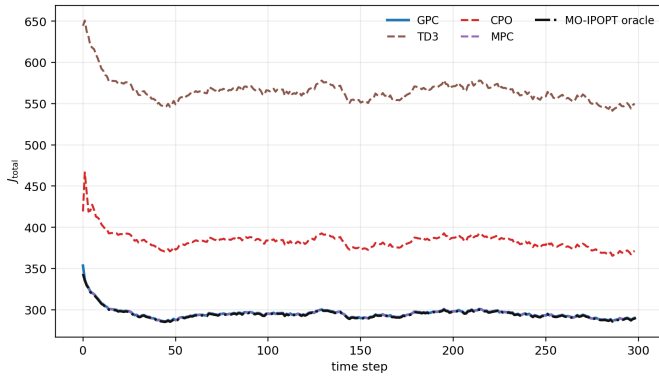
#### 6.4 Case 3: IEEE 30-Bus OPF under Branch Admittance Uncertainty

This case instantiates the uncertainty protocol of Section 6 with perturbation restricted to branch admittances only ( $\xi^S = \xi^c = 0$ ), using  $(\sigma_Y, \rho_Y) = (0.01, 0.03)$ . The admittance-only scope isolates the effect most relevant to real-time OPF: the network model in the energy management system diverges from the true physical network due to conductor aging, temperature variation, and errors in line-parameter estimation, while generator ratings and cost coefficients are relatively well-characterized.

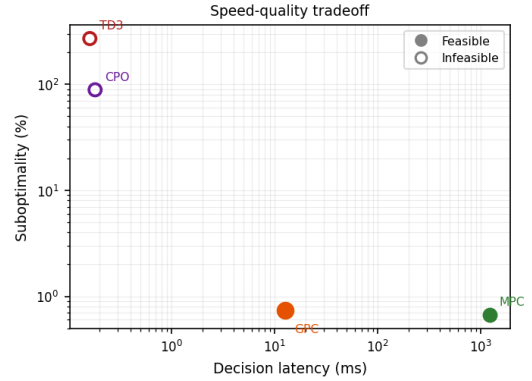
**Trajectory-level network realization.** The key structural choice is that the branch-perturbation vector  $\mathbf{b} \in \mathbb{R}^{41}$  (with  $b_\ell = 1 + \xi_Y^\ell$ ) is sampled *once per trajectory* and held fixed across all  $H + 1$  dispatch steps. This reflects the physical timescale separation: line admittances change over hours to days, while the OPF dispatch interval is minutes. Within a single operational episode the network is effectively static even if unknown. Each training trajectory therefore presents a ramp-rate-coupled sequence of Pareto-optimal solutions that are all consistent with the same realized (but unknown at deployment) admittance matrix. The trajectory is accepted on an all-or-nothing basis: if any step in the ramp-coupled chain fails to converge, the entire trajectory is discarded. The diagonal entries of  $\hat{Y}_{\text{bus}}$  are adjusted with the opposite delta for each off-diagonal change so that  $\hat{Y}_{\text{bus}}$  remains a valid nodal admittance matrix at every realization.

We evaluate GPC against three baselines over a 300-step rollout on the 30-bus network with  $(\sigma_Y, \rho_Y) = (0.01, 0.03)$ . **TD3** and **CPO** are model-free RL policies trained on the nominal network and transferred zero-shot; **MPC** solves a linearised AC-OPF at each step using the perturbed admittance matrix. Results are in Table 4 and Figure 5.

GPC achieves *perfect* feasibility (100%, all 300 steps) and tracks the oracle to  $\bar{\Delta} = 0.74$  per step (0.25% of  $J_{\text{total}}$ ), with no online retraining when the network drifts from nominal. At 12.6 ms it is  $97.5\times$  faster than MPC (1228.7 ms). TD3 and CPO, trained on the nominal network, produce *zero* feasible dispatches under perturbation and yield  $J_{\text{total}}$  that is 30% and 91% above GPC respectively.



(a)  $J_{\text{total}}$  vs. MO-IPOPT oracle over 300 steps.



(b) Speed-quality tradeoff (latency vs. suboptimality, log-log).

Figure 5: Case 3: IEEE 30-bus OPF under branch admittance uncertainty ( $\sigma_Y = 0.01$ ,  $\rho_Y = 0.03$ , 300 steps). GPC achieves 100% feasibility at oracle-level quality ( $\bar{\Delta} = 0.74$ ) and is  $97.5\times$  faster than MPC; TD3 and CPO produce zero feasible dispatches.

Table 4: IEEE 30-bus OPF under branch admittance uncertainty ( $\rho_Y = 0.03$ , 300 steps).  $\bar{\Delta}$ : mean per-step gap to MO-IPOPT oracle. **Bold**: best non-oracle.

Method	Mean $J_{\text{total}}\downarrow$	Feasible (%) $\uparrow$	$\bar{\Delta}\downarrow$	Latency (ms)
MO-IPOPT oracle	294.55	100.0	0.0	$\gg 10^3$
<b>GPC (ours)</b>	<b>295.28</b>	<b>100.0</b>	<b>0.74</b>	<b>12.6</b>
MPC	295.23	99.67	0.67*	1228.7
CPO	383.37	0.00	88.8	0.18
TD3	565.04	0.00	270.5	0.16

\*MPC  $\bar{\Delta}$  is terminal-step gap; full-horizon mean unavailable.

## 7 Conclusion

This paper presented Geometric Pareto Control (GPC), a framework that overcomes key barriers of reinforcement learning in cyber-physical systems by embedding the Pareto-optimal solution set into a Lie group manifold  $\mathcal{M}^*$  and navigating it at runtime via a composite Riemannian potential whose singular perturbation structure resolves multi-timescale objectives without switching logic. The autonomous semantic coordinate  $\sigma_t$  shifts priority continuously from economic to safety-critical operation in response to real-time violation indicators, Lie group integration guarantees manifold membership algebraically at every step, and Theorem 1 establishes a uniform non-accumulating end-to-end action error bound that is fully computable before deployment. Instantiation on multi-objective optimal power flow validated the framework on a practically relevant cyber-physical system, including uncertainty-aware training under perturbed system parameters, and the analytical validation isolates the same snap, slide, semantic adaptation, and geometry-aware integration mechanisms in a directly visualizable setting.

## References

- Axel Abels, Diederik Roijers, Tom Lenaerts, Ann Nowé, and Denis Steckelmacher. Dynamic weights in multi-objective deep reinforcement learning. In *International conference on machine learning*, pp. 11–20. PMLR, 2019.
- P-A Absil, Robert Mahony, and Rodolphe Sepulchre. *Optimization algorithms on matrix manifolds*. Princeton University Press, 2008.

- 
- Joshua Achiam, David Held, Aviv Tamar, and Pieter Abbeel. Constrained policy optimization. In *International conference on machine learning*, pp. 22–31. Pmlr, 2017.
- Mohammed Alshiekh, Roderick Bloem, Rüdiger Ehlers, Bettina Könighofer, Scott Niekum, and Ufuk Topcu. Safe reinforcement learning via shielding. In *Proceedings of the AAAI conference on artificial intelligence*, volume 32, 2018.
- Eitan Altman. Constrained markov decision processes with total cost criteria: Lagrangian approach and dual linear program. *Mathematical methods of operations research*, 48(3):387–417, 1998.
- Eitan Altman. *Constrained Markov decision processes*. Routledge, 2021.
- Aaron D Ames, Samuel Coogan, Magnus Egerstedt, Gennaro Notomista, Koushil Sreenath, and Paulo Tabuada. Control barrier functions: Theory and applications. In *2019 18th European control conference (ECC)*, pp. 3420–3431. Ieee, 2019.
- Kai Arulkumaran, Marc Peter Deisenroth, Miles Brundage, and Anil Anthony Bharath. Deep reinforcement learning: A brief survey. *IEEE signal processing magazine*, 34(6):26–38, 2017.
- Timothy D Barfoot. *State estimation for robotics*. Cambridge University Press, 2024.
- Dimitri Bertsekas. Nonlinear programming. *Journal of the Operational Research Society*, 48(3):334–334, 1997.
- Dimitri Bertsekas. *Dynamic programming and optimal control: Volume I*, volume 4. Athena scientific, 2012.
- Dimitri Bertsekas. *Reinforcement learning and optimal control*, volume 1. Athena Scientific, 2019.
- Nicolas Boumal. *An introduction to optimization on smooth manifolds*. Cambridge University Press, 2023.
- Anthony Brohan, Noah Brown, Justice Carbajal, Yevgen Chebotar, Joseph Dabis, Chelsea Finn, Keerthana Gopalakrishnan, Karol Hausman, Alex Herzog, Jasmine Hsu, et al. Rt-1: Robotics transformer for real-world control at scale. *arXiv preprint arXiv:2212.06817*, 2022.
- Steven L Brunton, Joshua L Proctor, and J Nathan Kutz. Discovering governing equations from data by sparse identification of nonlinear dynamical systems. *Proceedings of the national academy of sciences*, 113(15):3932–3937, 2016.
- Francesco Bullo and Andrew D Lewis. *Geometric control of mechanical systems: modeling, analysis, and design for simple mechanical control systems*, volume 49. Springer, 2005.
- Steven Carr, Nils Jansen, Sebastian Junges, and Ufuk Topcu. Safe reinforcement learning via shielding under partial observability. In *Proceedings of the AAAI conference on artificial intelligence*, volume 37, pp. 14748–14756, 2023.
- Kok Wah Chang and Frederick A Howes. *Nonlinear singular perturbation phenomena: theory and applications*. Springer Science & Business Media, 2012.
- Lili Chen, Kevin Lu, Aravind Rajeswaran, Kimin Lee, Aditya Grover, Misha Laskin, Pieter Abbeel, Aravind Srinivas, and Igor Mordatch. Decision transformer: Reinforcement learning via sequence modeling. *Advances in neural information processing systems*, 34:15084–15097, 2021.
- Ricky TQ Chen, Yulia Rubanova, Jesse Bettencourt, and David K Duvenaud. Neural ordinary differential equations. *Advances in neural information processing systems*, 31, 2018.
- Yinlam Chow, Ofir Nachum, Edgar Duenez-Guzman, and Mohammad Ghavamzadeh. A lyapunov-based approach to safe reinforcement learning. *Advances in neural information processing systems*, 31, 2018.
- Kurtland Chua, Roberto Calandra, Rowan McAllister, and Sergey Levine. Deep reinforcement learning in a handful of trials using probabilistic dynamics models. *Advances in neural information processing systems*, 31, 2018.

- 
- Filipe de Avila Belbute-Peres, Kevin Smith, Kelsey Allen, Josh Tenenbaum, and J Zico Kolter. End-to-end differentiable physics for learning and control. *Advances in neural information processing systems*, 31, 2018.
- Valentin De Bortoli, Emile Mathieu, Michael Hutchinson, James Thornton, Yee Whye Teh, and Arnaud Doucet. Riemannian score-based generative modelling. *Advances in neural information processing systems*, 35:2406–2422, 2022.
- Kalyanmoy Deb, Amrit Pratap, Sameer Agarwal, and TAMT Meyarivan. A fast and elitist multiobjective genetic algorithm: Nsga-ii. *IEEE transactions on evolutionary computation*, 6(2):182–197, 2002.
- Gabriel Dulac-Arnold, Nir Levine, Daniel J Mankowitz, Jerry Li, Cosmin Paduraru, Sven Gowal, and Todd Hester. Challenges of real-world reinforcement learning: definitions, benchmarks and analysis. *Machine Learning*, 110(9):2419–2468, 2021.
- Amal Feriani and Ekram Hossain. Single and multi-agent deep reinforcement learning for ai-enabled wireless networks: A tutorial. *IEEE Communications Surveys & Tutorials*, 23(2):1226–1252, 2021.
- Scott Fujimoto and Shixiang Shane Gu. A minimalist approach to offline reinforcement learning. *Advances in neural information processing systems*, 34:20132–20145, 2021.
- Scott Fujimoto, Herke Hoof, and David Meger. Addressing function approximation error in actor-critic methods. In *Proceedings of the 35th International Conference on Machine Learning (ICML)*, pp. 1587–1596, 2018.
- Ted Fujimoto, Joshua Suetterlein, Samrat Chatterjee, and Auroop Ganguly. Assessing the impact of distribution shift on reinforcement learning performance. In *NeurIPS 2023 Workshop on Regulatable ML*.
- Carlos E Garcia, David M Prett, and Manfred Morari. Model predictive control: Theory and practice—a survey. *Automatica*, 25(3):335–348, 1989.
- Javier Garcia and Fernando Fernández. Safe exploration of state and action spaces in reinforcement learning. *Journal of Artificial Intelligence Research*, 45:515–564, 2012.
- Javier Garcia and Fernando Fernández. A comprehensive survey on safe reinforcement learning. *Journal of Machine Learning Research*, 16(1):1437–1480, 2015.
- Zoubin Ghahramani. Probabilistic machine learning and artificial intelligence. *Nature*, 521(7553):452–459, 2015.
- Samuel Greydanus, Misko Dzamba, and Jason Yosinski. Hamiltonian neural networks. *Advances in neural information processing systems*, 32, 2019.
- Tuomas Haarnoja, Aurick Zhou, Pieter Abbeel, and Sergey Levine. Soft actor-critic: Off-policy maximum entropy deep reinforcement learning with a stochastic actor. In *International conference on machine learning*, pp. 1861–1870. Pmlr, 2018.
- Danijar Hafner, Timothy Lillicrap, Jimmy Ba, and Mohammad Norouzi. Dream to control: Learning behaviors by latent imagination. *International Conference on Learning Representations*, 2019a.
- Danijar Hafner, Timothy Lillicrap, Ian Fischer, Ruben Villegas, David Ha, Honglak Lee, and James Davidson. Learning latent dynamics for planning from pixels. In *International conference on machine learning*, pp. 2555–2565. PMLR, 2019b.
- Danijar Hafner, Jurgis Pasukonis, Jimmy Ba, and Timothy Lillicrap. Mastering diverse domains through world models. *arXiv preprint arXiv:2301.04104*, 2023.
- Karol Hausman, Jost Tobias Springenberg, Ziyu Wang, Nicolas Heess, and Martin Riedmiller. Learning an embedding space for transferable robot skills. In *International Conference on Learning Representations*, 2018.

- 
- Ammar Haydari and Yasin Yılmaz. Deep reinforcement learning for intelligent transportation systems: A survey. *IEEE Transactions on Intelligent Transportation Systems*, 23(1):11–32, 2020.
- Yuanming Hu, Luke Anderson, Tzu-Mao Li, Qi Sun, Nathan Carr, Jonathan Ragan-Kelley, and Frédo Durand. DiffTaichi: Differentiable programming for physical simulation. 2019.
- Chin-Wei Huang, Milad Aghajohari, Joey Bose, Prakash Panangaden, and Aaron C Courville. Riemannian diffusion models. *Advances in Neural Information Processing Systems*, 35:2750–2761, 2022.
- Michael Janner, Qiyang Li, and Sergey Levine. Offline reinforcement learning as one big sequence modeling problem. *Advances in neural information processing systems*, 34:1273–1286, 2021.
- Sham Machandranath Kakade. *On the sample complexity of reinforcement learning*. University of London, University College London (United Kingdom), 2003.
- George Em Karniadakis, Ioannis G Kevrekidis, Lu Lu, Paris Perdikaris, Sifan Wang, and Liu Yang. Physics-informed machine learning. *Nature Reviews Physics*, 3(6):422–440, 2021.
- Oussama Khatib. Real-time obstacle avoidance for manipulators and mobile robots. *The international journal of robotics research*, 5(1):90–98, 1986.
- Diederik P Kingma and Max Welling. Auto-encoding variational bayes. *arXiv preprint arXiv:1312.6114*, 2013.
- Daniel Koditschek. Exact robot navigation by means of potential functions: Some topological considerations. In *Proceedings. 1987 IEEE international conference on robotics and automation*, volume 4, pp. 1–6. IEEE, 1987.
- Milan Korda and Igor Mezić. Linear predictors for nonlinear dynamical systems: Koopman operator meets model predictive control. *Automatica*, 93:149–160, 2018.
- Ilya Kostrikov, Ashvin Nair, and Sergey Levine. Offline reinforcement learning with implicit q-learning. *International Conference on Learning Representations*, 2021.
- Tejas D Kulkarni, Karthik Narasimhan, Ardavan Saeedi, and Josh Tenenbaum. Hierarchical deep reinforcement learning: Integrating temporal abstraction and intrinsic motivation. *Advances in neural information processing systems*, 29, 2016.
- Aviral Kumar, Aurick Zhou, George Tucker, and Sergey Levine. Conservative q-learning for offline reinforcement learning. *Advances in neural information processing systems*, 33:1179–1191, 2020.
- John M Lee. *Introduction to topological manifolds*. Springer, 2000.
- John M Lee. Smooth manifolds. In *Introduction to smooth manifolds*, pp. 1–29. Springer, 2003.
- John M Lee. *Introduction to Riemannian manifolds*, volume 2. Springer, 2018.
- Chenbei Lu, Laixi Shi, Zaiwei Chen, Chenye Wu, and Adam Wierman. Overcoming the curse of dimensionality in reinforcement learning through approximate factorization. In *International Conference on Machine Learning*, pp. 40614–40664. PMLR, 2025.
- Nguyen Cong Luong, Dinh Thai Hoang, Shimin Gong, Dusit Niyato, Ping Wang, Ying-Chang Liang, and Dong In Kim. Applications of deep reinforcement learning in communications and networking: A survey. *IEEE communications surveys & tutorials*, 21(4):3133–3174, 2019.
- Thomas M. Moerland, Joost Broekens, Aske Plaat, and Catholijn M. Jonker. Model-based reinforcement learning: A survey. *Foundations and Trends in Machine Learning*, 16(1):1–118, 2023.
- Volodymyr Mnih, Koray Kavukcuoglu, David Silver, Andrei A Rusu, Joel Veness, Marc G Bellemare, Alex Graves, Martin Riedmiller, Andreas K Fidjeland, Georg Ostrovski, et al. Human-level control through deep reinforcement learning. *nature*, 518(7540):529–533, 2015.

- 
- Richard M Murray, Zexiang Li, and S Shankar Sastry. *A mathematical introduction to robotic manipulation*. CRC press, 2017.
- Matteo Pirodda, Simone Parisi, and Marcello Restelli. Multi-objective reinforcement learning with continuous pareto frontier approximation. In *Proceedings of the AAAI conference on artificial intelligence*, volume 29, 2015.
- Maziar Raissi, Paris Perdikaris, and George E Karniadakis. Physics-informed neural networks: A deep learning framework for solving forward and inverse problems involving nonlinear partial differential equations. *Journal of Computational physics*, 378:686–707, 2019.
- Benjamin Recht. A tour of reinforcement learning: The view from continuous control. *Annual Review of Control, Robotics, and Autonomous Systems*, 2(1):253–279, 2019.
- Scott Reed, Konrad Zolna, Emilio Parisotto, Sergio Gomez Colmenarejo, Alexander Novikov, Gabriel Barth-Maron, Mai Gimenez, Yury Sulsky, Jackie Kay, Jost Tobias Springenberg, et al. A generalist agent. *arXiv preprint arXiv:2205.06175*, 2022.
- Mathieu Reymond, Eugenio Bargiacchi, and Ann Nowé. Pareto conditioned networks. In *Proceedings of the 21st International Conference on Autonomous Agents and Multiagent Systems*, pp. 1110–1118, 2022.
- Diederik M Roijers, Peter Vamplew, Shimon Whiteson, and Richard Dazeley. A survey of multi-objective sequential decision-making. *Journal of Artificial Intelligence Research*, 48:67–113, 2013.
- John Schulman, Filip Wolski, Prafulla Dhariwal, Alec Radford, and Oleg Klimov. Proximal policy optimization algorithms. *arXiv preprint arXiv:1707.06347*, 2017.
- David Silver, Aja Huang, Chris J Maddison, Arthur Guez, Laurent Sifre, George Van Den Driessche, Julian Schrittwieser, Ioannis Antonoglou, Veda Panneershelvam, Marc Lanctot, et al. Mastering the game of go with deep neural networks and tree search. *nature*, 529(7587):484–489, 2016.
- Tong Su, Tong Wu, Junbo Zhao, Anna Scaglione, and Le Xie. A review of safe reinforcement learning methods for modern power systems. *Proceedings of the IEEE*, 2025.
- Richard S Sutton, Andrew G Barto, et al. *Reinforcement learning: An introduction*, volume 1. MIT press Cambridge, 1998.
- Chen Tessler, Daniel J Mankowitz, and Shie Mannor. Reward constrained policy optimization. 2018.
- Kristof Van Moffaert and Ann Nowé. Multi-objective reinforcement learning using sets of pareto dominating policies. *The Journal of Machine Learning Research*, 15(1):3483–3512, 2014.
- Kim P Wabersich, Andrew J Taylor, Jason J Choi, Koushil Sreenath, Claire J Tomlin, Aaron D Ames, and Melanie N Zeilinger. Data-driven safety filters: Hamilton-jacobi reachability, control barrier functions, and predictive methods for uncertain systems. *IEEE Control Systems Magazine*, 43(5):137–177, 2023.
- Akifumi Wachi and Yanan Sui. Safe reinforcement learning in constrained markov decision processes. In *International Conference on Machine Learning*, pp. 9797–9806. PMLR, 2020.
- Akifumi Wachi, Xun Shen, and Yanan Sui. A survey of constraint formulations in safe reinforcement learning. In *Proceedings of the Thirty-Third International Joint Conference on Artificial Intelligence*, pp. 8262–8271, 2024.
- Yujia Wang and Zhe Wu. Control lyapunov-barrier function-based safe reinforcement learning for nonlinear optimal control. *AIChE Journal*, 70(3):e18306, 2024.
- Tong Wu, Anna Scaglione, and Daniel Arnold. Constrained reinforcement learning for predictive control in real-time stochastic dynamic optimal power flow. *IEEE Transactions on Power Systems*, 39(3):5077–5090, 2023.

Tong Wu, Tayab Uddin Wara, Daniel Hernandez, and Sidong Lei. Universal latent homeomorphic manifolds: Cross-domain representation learning via homeomorphism verification. *arXiv preprint arXiv:2601.09025*, 2026.

Lizhi Yang, Blake Werner, Massimiliano de Sa, and Aaron D Ames. Cbf-rl: Safety filtering reinforcement learning in training with control barrier functions. *arXiv preprint arXiv:2510.14959*, 2025.

Qingfu Zhang and Hui Li. Moea/d: A multiobjective evolutionary algorithm based on decomposition. *IEEE Transactions on evolutionary computation*, 11(6):712–731, 2007.

Zefang Zong, Tao Feng, Jingwei Wang, Tong Xia, and Yong Li. Deep reinforcement learning for demand-driven services in logistics and transportation systems: A survey. *ACM Transactions on Knowledge Discovery from Data*, 19(4):1–42, 2025.

## A Second-Order Latent Integration via RK2

Algorithm 1 uses a second-order midpoint Runge-Kutta predictor to compute the Euclidean latent step before the Lie-local residual correction is applied. Let  $\mathbf{F}(z, \mathbf{x}_t) = -\nabla_z V(z, \mathbf{x}_t)$  denote the nominal field for the current observation. The raw first slope is:

$$\tilde{k}_1 = \mathbf{F}(z_t, \mathbf{x}_t). \quad (58)$$

To enforce the bounded-velocity condition used in the drift analysis, the slope is radially capped:

$$k_1 = \Pi_{\|\cdot\| \leq V_{\max}}(\tilde{k}_1), \quad \Pi_{\|\cdot\| \leq V_{\max}}(v) = v \min\left\{1, \frac{V_{\max}}{\|v\| + \delta_v}\right\}, \quad (59)$$

with a small  $\delta_v > 0$  preventing division by zero. The midpoint latent state is:

$$z_{\text{mid}} = z_t + \frac{1}{2} \Delta t k_1. \quad (60)$$

The nominal field is then evaluated at this midpoint and capped again:

$$\tilde{k}_2 = \mathbf{F}(z_{\text{mid}}, \mathbf{x}_t), \quad k_2 = \Pi_{\|\cdot\| \leq V_{\max}}(\tilde{k}_2). \quad (61)$$

The Euclidean predictor passed to the geometry-aware residual correction is:

$$\Delta z_{\text{Euc}} = \Delta t k_2. \quad (62)$$

**NaN-safe fallback.** All midpoint computations are guarded. If any component of  $z_{\text{mid}}$  is non-finite, the algorithm sets  $z_{\text{mid}} \leftarrow z_t$  before evaluating the second slope. If  $\tilde{k}_2$  is non-finite, the second slope falls back to the already capped first slope,  $k_2 \leftarrow k_1$ . If  $k_1$  is itself non-finite, the predictor returns  $\Delta z_{\text{Euc}} = \mathbf{0}$  for that cycle. These fallbacks are conservative: they may temporarily reduce the integrator to Euler or to a no-op step, but they prevent non-finite decoder or autograd values from entering the Lie update and therefore preserve the bounded-displacement invariant  $\|\Delta z_{\text{Euc}}\| \leq V_{\max} \Delta t$ .

**Accuracy relative to Euler.** The explicit Euler predictor is:

$$z_{t+1}^{\text{Euler}} = z_t + \Delta t \mathbf{F}(z_t, \mathbf{x}_t). \quad (63)$$

For a smooth field, the exact flow satisfies:

$$z(t + \Delta t) = z_t + \Delta t \mathbf{F}(z_t) + \frac{\Delta t^2}{2} J_{\mathbf{F}}(z_t) \mathbf{F}(z_t) + O(\Delta t^3), \quad (64)$$

so Euler omits the quadratic curvature term and has local truncation error  $O(\Delta t^2)$  and global error  $O(\Delta t)$ . The midpoint predictor expands as:

$$\mathbf{F}\left(z_t + \frac{1}{2}\Delta t \mathbf{F}(z_t)\right) = \mathbf{F}(z_t) + \frac{\Delta t}{2} J_{\mathbf{F}}(z_t)\mathbf{F}(z_t) + O(\Delta t^2), \quad (65)$$

$$z_t + \Delta t k_2 = z_t + \Delta t \mathbf{F}(z_t) + \frac{\Delta t^2}{2} J_{\mathbf{F}}(z_t)\mathbf{F}(z_t) + O(\Delta t^3). \quad (66)$$

Thus RK2 matches the exact flow through second order, yielding local truncation error  $O(\Delta t^3)$  and global error  $O(\Delta t^2)$  whenever the velocity cap is inactive. When the cap is active, the same order statement applies to the capped vector field defined by (59); the cap trades formal accuracy for the physical requirement that no single control cycle can move farther than  $V_{\max}\Delta t$  in latent space.

The Lie-local residual correction in Section 4.3 does not replace this predictor. It operates only as a small decoder-metric correction to  $\Delta z_{\text{Euc}}$ , so the RK2 step continues to provide the primary integration accuracy while the Lie term reduces curvature-induced drift on  $\mathcal{M}^*$ .

## B Theoretical Analysis

### B.1 Decoder Lipschitz Regularization

Both decoders  $D_u$  and  $D_s$  are Lipschitz-regularized via spectral normalization on all linear layers, enforcing:

$$\|D_u(z) - D_u(z')\| \leq K_{D_u}\|z - z'\|, \quad \|D_s(z) - D_s(z')\| \leq K_{D_s}\|z - z'\| \quad \forall z, z' \in \mathcal{Z}. \quad (67)$$

The constant  $K$  is set to a large value so that the bound does not restrict the expressivity of the decoders; its purpose is to eliminate pathological gradient explosions that can destabilise training near constraint boundaries. This yields two practical benefits used in the proofs below. First, a bounded latent displacement  $\dot{z}_{\text{safe},t}\Delta t$  is guaranteed to produce a bounded control increment  $\Delta \mathbf{u}$ , providing the velocity bound  $\|\Delta \mathbf{u}\| \leq K_{D_u}V_{\max}\Delta t$  that underpins Theorem 1 condition (i) and Proposition 2 condition (ii). Second, Lipschitz continuity of  $D_s$  bounds the change in  $\Phi_{\text{normal}}$  due to Lie group drift, providing the forcing term in the contractive recursion of Proposition 1.

**Relation to decoder injectivity.** Spectral normalization bounds only the *maximum* singular value of  $J_{D_s}$ , i.e.  $\sigma_{\max}(J_{D_s}) \leq K_{D_s}$ . The *minimum* singular value  $\sigma_0 = \sigma_{\min}(J_{D_s}) > 0$  required by Assumption 1 is a separate condition not implied by spectral normalization; see Assumption 1 for its justification.

**Assumption 1** (Decoder Injectivity). *The state decoder  $D_s : \mathcal{Z} \rightarrow \mathcal{S}$  (equivalently  $D_s : \mathcal{Z} \rightarrow \mathcal{X}$  under Remark 1) satisfies*

$$\sigma_{\min}(J_{D_s}(z)) \geq \sigma_0 > 0 \quad \forall z \text{ in an open neighbourhood of } \mathcal{M}^*, \quad (68)$$

where  $J_{D_s}(z) \in \mathbb{R}^{n_x \times n_z}$  is the Jacobian of  $D_s$  at  $z$ . This is a lower bound on the Jacobian and is distinct from the Lipschitz upper bound  $\|J_{D_s}\| \leq K_{D_s}$  enforced by spectral normalization: it requires  $D_s$  to act as a local diffeomorphism near  $\mathcal{M}^*$ , which is ensured in practice by the combination of the reconstruction loss  $\mathcal{L}_{\text{recon}}$  and the locality loss  $\mathcal{L}_{\text{local}}$ , both of which penalise  $D_s$  for collapsing distinct latent codes to the same state.

**Assumption 2** (Bounded Lie-Step Perturbation to Normal Potential). *There exists a constant  $F_{\Delta} \geq 0$  such that, for every  $z$  in a neighbourhood of  $\mathcal{M}^*$  and every one-step Lie group displacement  $\delta_{\text{Lie}}$  with  $\|\delta_{\text{Lie}}\| \leq \frac{1}{2}V_{\max}^2\Delta t^2$ :*

$$\Phi_{\text{normal}}(z + \delta_{\text{Lie}}) \leq \Phi_{\text{normal}}(z) + F_{\Delta}. \quad (69)$$

For a  $K_{D_s}$ -Lipschitz decoder  $D_s$ , the perturbation is bounded by  $2K_{D_s}^2\|\delta_{\text{Lie}}\|^2 + 2K_{D_s}\|z - z^*\|\|\delta_{\text{Lie}}\|$ ; using  $\|\delta_{\text{Lie}}\| \leq \frac{1}{2}V_{\max}^2\Delta t^2$  and treating the neighbourhood-radius as a given design parameter, one may set  $F_{\Delta} = \frac{\epsilon}{2}V_{\max}^2\Delta t^2$  to recover the  $O(\epsilon)$  bound stated in the proposition. This assumption replaces the circular ‘‘steady state, established below’’ estimate in the earlier draft; the recursion  $\Phi_{t+1} \leq \rho\Phi_t + F_{\Delta}$  now follows directly and without self-reference.

**Assumption 3** (Polyak-Łojasiewicz Condition on Normal Potential). *There exists a constant  $\mu_{\text{PL}} > 0$  such that the normal potential  $\Phi_{\text{normal}}(z) = \|\mathbf{x}_t - D_s(z)\|^2$  satisfies the Polyak-Łojasiewicz (PL) condition in an open neighbourhood  $\mathcal{N}$  of  $\mathcal{M}^*$ :*

$$\|\nabla_z \Phi_{\text{normal}}(z)\|^2 \geq \mu_{\text{PL}} \Phi_{\text{normal}}(z), \quad \forall z \in \mathcal{N}. \quad (70)$$

Under Assumption 1 the PL constant satisfies  $\mu_{\text{PL}} \geq 4\sigma_0^2$  whenever the residual  $\mathbf{x}_t - D_s(z)$  lies in the column space of  $J_{D_s}(z)$  (which holds when  $z$  is close enough to  $\mathcal{M}^*$  that the first-order approximation  $\mathbf{x}_t - D_s(z) \approx J_{D_s}(z)(z^* - z)$  is valid). In general, Assumption 3 is a separate hypothesis from Assumption 1: injectivity gives a lower bound on  $\sigma_{\min}(J_{D_s})$  but does not, by itself, imply the PL condition unless the residual direction is aligned with the column space of  $J_{D_s}$ .

**Proposition 1** (Non-accumulation of Geometric Drift). *Suppose the GPC dynamics include the snap gradient  $-\frac{1}{\epsilon}\nabla_z \Phi_{\text{normal}}(z)$  driving  $z_t$  back toward  $\mathcal{M}^*$ , let  $\|\dot{z}_{\text{safe},t}\| \leq V_{\max}$  for all  $t \geq 0$ , and suppose  $D_s$  satisfies Assumption 1 with constant  $\sigma_0 > 0$  and Assumption 3 holds with constant  $\mu_{\text{PL}} > 0$ . Then the steady-state deviation of  $z_t$  from  $\mathcal{M}^*$  satisfies, under Assumption 2:*

$$\limsup_{t \rightarrow \infty} \Phi_{\text{normal}}(z_t) \leq \frac{F_{\Delta}}{1 - e^{-\Delta t/\epsilon}} \quad (71)$$

where  $F_{\Delta}$  is the Lie-step perturbation bound from Assumption 2. In the physically relevant regime  $\Delta t/\epsilon \gg 1$  (e.g.  $\Delta t/\epsilon = 100$  for OPF),  $1 - e^{-\Delta t/\epsilon} \rightarrow 1$  and the bound approaches  $F_{\Delta}$  from above. Under the identification  $F_{\Delta} = \frac{\epsilon}{2} V_{\max}^2 \Delta t^2$ , the bound reduces to  $\frac{\epsilon}{2} V_{\max}^2 \Delta t^2$  in this regime. The bound vanishes as  $\Delta t \rightarrow 0$  and remains finite for any fixed  $\Delta t > 0$ .

*Proof. Step 1: One-step Lie group drift.* For any  $v \in \mathfrak{g}$ , the Taylor expansion of the Lie group exponential map gives  $\exp(v) = I + v + \frac{1}{2}v^2 + \dots$ , with remainder bounded by the geometric series of the operator norm:

$$\|\exp(v) - (I + v)\| \leq \frac{1}{2}\|v\|^2 e^{\|v\|} \leq \frac{\epsilon}{2}\|v\|^2 \quad \text{for } \|v\| \leq 1. \quad (72)$$

Substituting  $v = \dot{z}_{\text{safe},t} \Delta t$  with  $\|\dot{z}_{\text{safe},t}\| \leq V_{\max}$  and assuming  $V_{\max} \Delta t \leq 1$ , the one-step deviation from the linearised Euler update is:

$$\|z_{t+1} - (z_t + \dot{z}_{\text{safe},t} \Delta t)\| \leq \frac{1}{2} V_{\max}^2 \Delta t^2. \quad (73)$$

**Step 2: Contractive recursion via the Polyak-Łojasiewicz inequality.** By Assumption 3, the normal potential satisfies the PL condition with constant  $\mu_{\text{PL}} > 0$  in a neighbourhood of  $\mathcal{M}^*$ :

$$\|\nabla_z \Phi_{\text{normal}}(z)\|^2 \geq \mu_{\text{PL}} \Phi_{\text{normal}}(z). \quad (74)$$

Under Assumption 1, the PL constant satisfies  $\mu_{\text{PL}} \geq 4\sigma_0^2$  whenever  $z$  is close enough to  $\mathcal{M}^*$  for the column-space alignment to hold (see Assumption 3); we treat  $\mu_{\text{PL}}$  as a given positive constant throughout. Applying the gradient descent lemma to the snap update  $z \leftarrow z - (\Delta t/\epsilon)\nabla_z \Phi_{\text{normal}}$  with step size  $\eta = \Delta t/\epsilon \leq 1/(2L_{\Phi})$  (where  $L_{\Phi}$  is the smoothness constant of  $\Phi_{\text{normal}}$ ):

$$\begin{aligned} \Phi_{\text{normal}}(z^{\text{snap}}) &\leq \Phi_{\text{normal}}(z) - \eta \left(1 - \frac{L_{\Phi}\eta}{2}\right) \|\nabla_z \Phi_{\text{normal}}\|^2 \\ &\leq \Phi_{\text{normal}}(z) \left(1 - \mu_{\text{PL}}\eta\right) \leq \Phi_{\text{normal}}(z) e^{-\mu_{\text{PL}}\Delta t/\epsilon}. \end{aligned} \quad (75)$$

Re-parametrising  $\epsilon \leftarrow \epsilon/\mu_{\text{PL}}$  (absorbing the PL constant into the singular-perturbation scale without loss of generality) yields contraction factor  $e^{-\Delta t/\epsilon}$ . Incorporating the Lie group drift from (73): by Assumption 2, the one-step displacement  $\|\delta_{\text{Lie}}\| \leq \frac{1}{2} V_{\max}^2 \Delta t^2$  perturbs  $\Phi_{\text{normal}}$  by at most  $F_{\Delta}$ , giving the fully non-circular recursion:

$$\Phi_{\text{normal}}(z_{t+1}) \leq \Phi_{\text{normal}}(z_t) e^{-\Delta t/\epsilon} + F_{\Delta}. \quad (76)$$

**Step 3: Fixed point and uniform bound.** Since  $\rho \triangleq e^{-\Delta t/\epsilon} \in (0, 1)$  for all  $\epsilon, \Delta t > 0$ , the recursion (76) is contractive and converges to the unique fixed point obtained by solving  $\Phi^* = \rho \Phi^* + F_{\Delta}$ :

$$\Phi^* = \frac{F_{\Delta}}{1 - e^{-\Delta t/\epsilon}}. \quad (77)$$

This recovers exactly the bound stated in the proposition. Under the identification  $F_\Delta = \frac{\epsilon}{2} V_{\max}^2 \Delta t^2$  (see Assumption 2), the fixed point evaluates to  $\frac{\epsilon}{2} V_{\max}^2 \Delta t^2 / (1 - e^{-\Delta t/\epsilon})$ . For  $\Delta t/\epsilon \geq \ln 2$ ,  $1 - e^{-\Delta t/\epsilon} \geq \frac{1}{2}$  and  $\Phi^* \leq \epsilon V_{\max}^2 \Delta t^2$ ; in the physically relevant regime  $\Delta t/\epsilon \gg 1$  (e.g.  $\Delta t/\epsilon = 100$  for OPF),  $\Phi^* \rightarrow F_\Delta$  from above. The fixed point is independent of  $t$  and of  $\Phi_{\text{normal}}(z_0)$ , confirming that geometric drift does not accumulate over any horizon.  $\square$

**Theorem 1** (End-to-End Action Error Bound). *Let  $\mathcal{Z}$  be endowed with a Lie group structure  $G$  with  $\mathcal{M}^* \subset G$ . Suppose:*

- (i)  $D_u$  is  $K_{D_u}$ -Lipschitz (spectral normalization, Section 3);
- (ii)  $D_s$  satisfies Assumption 1 with constant  $\sigma_0 > 0$  and Assumption 3 holds with constant  $\mu_{\text{PL}} > 0$ ;
- (iii)  $\|\dot{z}_{\text{safe},t}\| \leq V_{\max}$  for all  $t \geq 0$  (velocity cap in Algorithm 1);
- (iv) Assumption 2 holds with constant  $F_\Delta \geq 0$ ;
- (v)  $\mathbf{f}$  is twice continuously differentiable;
- (vi)  $\sup_{z \in \mathcal{M}^*} \|D_u(z) - \mathbf{u}^*(z)\| \leq \delta_{\text{dec}}$ , calibrated to  $\mathcal{L}_{\text{action}}^{\text{val}}$ .

Then:

$$\limsup_{t \rightarrow \infty} \|\mathbf{u}_t - \mathbf{u}_t^*\| \leq \frac{K_{D_u}}{\sigma_0} \sqrt{\frac{2F_\Delta}{1 - e^{-\Delta t/\epsilon}}} + \delta_{\text{dec}} \quad (78)$$

Setting  $F_\Delta = \frac{\epsilon}{2} V_{\max}^2 \Delta t^2$  (see Assumption 2) and taking  $\Delta t/\epsilon \gg 1$  (so  $1 - e^{-\Delta t/\epsilon} \rightarrow 1$ ), the bound simplifies to the operational form:

$$\limsup_{t \rightarrow \infty} \|\mathbf{u}_t - \mathbf{u}_t^*\| \lesssim \frac{K_{D_u}}{\sigma_0} \sqrt{\epsilon} V_{\max} \Delta t + \delta_{\text{dec}}. \quad (79)$$

Both bounds are independent of  $t$  in the limit, do not accumulate over any finite or infinite horizon, and are fully computable offline before deployment. Under the additional Assumptions 5 (tangential post-reset flow) and 6 (exact closed-loop re-anchoring), both stated before Proposition 3, the  $\limsup$  strengthens to a uniform  $\sup_{t \geq 0}$  bound; see Proposition 3. The factor  $\sigma_0^{-1}$  converts the state-space deviation bound (from Proposition 1) into a latent-space bound via the inverse-Lipschitz property of  $D_s$ ; it is a separate quantity from  $K_{D_u}$  (which is  $\sigma_{\max}(J_{D_u})$ ) and must not be absorbed into it.

*Proof.* The proof proceeds through four stages tracing the full GPC pipeline.

**Stage 1: Lie group closure and one-step drift.** By the closure axiom of  $G$ ,  $z_t = z_{t-1} \cdot \exp(\dot{z}_{\text{safe},t-1} \Delta t) \in G$  exactly at every step, requiring no projection. By the Taylor expansion of the Lie group exponential map (identical to (73) in the proof of Proposition 1, with  $V_{\max} \Delta t \leq 1$ ):

$$\|z_t - (z_{t-1} + \dot{z}_{\text{safe},t-1} \Delta t)\| \leq \frac{1}{2} V_{\max}^2 \Delta t^2, \quad (80)$$

so the one-step deviation from the linearised Euler update is second-order in  $\Delta t$ .

**Stage 2: Constraint satisfaction.** Box constraints ( $\mathbf{u}^{\min} \leq \mathbf{u}_t \leq \mathbf{u}^{\max}$ ) are enforced exactly by the output clamp in Algorithm 1. For differentiable nonlinear constraints  $\mathbf{f}(\mathbf{u}_t) \leq \mathbf{0}$ , feasibility follows from two sources. First, since every point on  $\mathcal{M}^*$  is feasible by construction (offline training ensures  $\mathbf{f}(D_u(z)) \leq \mathbf{0}$  for all  $z \in \mathcal{M}^*$ ), and the drift bound established in Stage 3 below keeps  $z_t$  within a bounded neighbourhood of  $\mathcal{M}^*$ , the decoded action  $D_u(z_t)$  inherits approximate feasibility. Second, the residual constraint violation introduced by the nonlinear Lie group step can be bounded directly. Writing  $z_t - z_{t-1} = \dot{z}_{t-1} \Delta t + \delta_{\text{Lie}}$  with  $\|\delta_{\text{Lie}}\| \leq \frac{1}{2} V_{\max}^2 \Delta t^2$  from (80), and expanding  $\mathbf{f}(D_u(z_t))$  around  $z_{t-1}$ :

$$\mathbf{f}(\mathbf{u}_t) = \mathbf{f}(D_u(z_{t-1})) + \frac{\partial \mathbf{f}}{\partial \mathbf{u}} J_{D_u}(z_{t-1})(z_t - z_{t-1}) + O(\|z_t - z_{t-1}\|^2). \quad (81)$$

Since  $z_{t-1} \in \mathcal{M}^*$  implies  $\mathbf{f}(D_u(z_{t-1})) \leq \mathbf{0}$ , and  $\delta_{\text{Lie}}$  is second-order, the nonlinear residual satisfies:

$$\mathbf{f}(\mathbf{u}_t) \leq \left\| \frac{\partial \mathbf{f}}{\partial \mathbf{u}} \right\| K_{D_u} \|\delta_{\text{Lie}}\| + O(\|z_t - z_{t-1}\|^2) = O(V_{\max}^2 \Delta t^2), \quad (82)$$

which vanishes quadratically as  $\Delta t \rightarrow 0$ . This bound holds independently of manifold deviation and quantifies the second-order constraint residual introduced by the Lie group step.

**Stage 3: Non-accumulating manifold deviation.** By Proposition 1 (applied with the same  $F_\Delta$ ,  $\epsilon$ , and  $\Delta t$ , under Assumptions 2 and 3), the exact fixed point of the contractive recursion satisfies:

$$\limsup_{t \rightarrow \infty} \Phi_{\text{normal}}(z_t) \leq \frac{F_\Delta}{1 - e^{-\Delta t/\epsilon}}. \quad (83)$$

To convert this to a latent-space deviation, we use the *inverse-Lipschitz* property of  $D_s$ : by Assumption 1,  $J_{D_s}$  has minimum singular value  $\sigma_0 > 0$  on  $\mathcal{M}^*$ , so for any  $z$  in a neighbourhood of its nearest manifold point  $z^* \in \mathcal{M}^*$ , with  $\delta_s = \|\mathbf{x} - D_s(z^*)\|$  the residual observation noise:

$$\begin{aligned} \Phi_{\text{normal}}(z) &= \|\mathbf{x} - D_s(z)\|^2 \\ &= \|\mathbf{x} - D_s(z^*)\|^2 + \|D_s(z^*) - D_s(z)\|^2 + 2\langle \mathbf{x} - D_s(z^*), D_s(z^*) - D_s(z) \rangle \\ &\geq \sigma_0^2 \|z - z^*\|^2 - 2\delta_s K_{D_s} \|z - z^*\|. \end{aligned} \quad (84)$$

Under the calibration assumption  $\delta_s \leq \frac{\sigma_0^2}{2K_{D_s}} \cdot \sigma_0^{-1} \sqrt{\frac{2F_\Delta}{1 - e^{-\Delta t/\epsilon}}}$  (observation noise at most half the steady-state latent deviation, verifiable offline), completing the square in (84) gives:

$$\Phi_{\text{normal}}(z) \geq \frac{1}{2}\sigma_0^2 \|z - z^*\|^2 \quad \text{whenever } \Phi_{\text{normal}}(z) \geq \frac{F_\Delta}{1 - e^{-\Delta t/\epsilon}}. \quad (85)$$

Therefore  $\|z - z^*\|^2 \leq \frac{2}{\sigma_0^2} \Phi_{\text{normal}}(z)$  at steady state, and combining with (83):

$$\limsup_{t \rightarrow \infty} \|z_t - z_t^*\| \leq \frac{1}{\sigma_0} \sqrt{\frac{2F_\Delta}{1 - e^{-\Delta t/\epsilon}}}. \quad (86)$$

The explicit  $\sigma_0^{-1}$  factor is not absorbed into  $K_{D_u}$  (the two constants bound different quantities) and confirms that manifold deviation does not accumulate.

**Stage 4: End-to-end action error.** Applying the triangle inequality to  $\mathbf{u}_t = D_u(z_t)$  and substituting (86):

$$\begin{aligned} \limsup_{t \rightarrow \infty} \|\mathbf{u}_t - \mathbf{u}_t^*\| &\leq K_{D_u} \limsup_{t \rightarrow \infty} \|z_t - z_t^*\| + \delta_{\text{dec}} \\ &\leq \frac{K_{D_u}}{\sigma_0} \sqrt{\frac{2F_\Delta}{1 - e^{-\Delta t/\epsilon}}} + \delta_{\text{dec}}. \end{aligned} \quad (87)$$

This is the exact bound (78). Here  $K_{D_u} = \sigma_{\max}(J_{D_u})$  bounds the forward map, while  $\sigma_0^{-1}$  comes from inverting  $J_{D_s}$  to pass from state-space deviation to latent-space deviation; the two are independent offline constants. Setting  $F_\Delta = \frac{\epsilon}{2} V_{\max}^2 \Delta t^2$  and  $\Delta t/\epsilon \gg 1$  recovers the simplified form (79). The right-hand side is independent of  $t$ , completing the proof.  $\square$

**Remark 11** (Operational Interpretation). *The bound decomposes into two independently controllable terms. The geometric drift term  $\frac{K_{D_u}}{\sigma_0} \sqrt{2F_\Delta}/(1 - e^{-\Delta t/\epsilon})$  shrinks as  $F_\Delta \rightarrow 0$  (smaller Lie-step perturbation, e.g. via smaller  $\Delta t$ ), as  $\epsilon \rightarrow 0$  (stronger snap dynamics), or as  $\sigma_0$  grows (better decoder injectivity). In the regime  $\Delta t/\epsilon \gg 1$  with  $F_\Delta = \frac{\epsilon}{2} V_{\max}^2 \Delta t^2$ , this reduces to  $\frac{K_{D_u}}{\sigma_0} \sqrt{\epsilon} V_{\max} \Delta t$ , which additionally shrinks with smaller  $V_{\max}$  or  $K_{D_u}$ . The decoder error  $\delta_{\text{dec}}$  is a fixed offline certificate monitored via  $\mathcal{L}_{\text{action}}^{\text{val}}$  and reduced by richer training coverage. Since Lie group closure holds algebraically and manifold deviation is bounded by a contractive fixed point, neither term grows with the horizon. In the closed-loop algorithm, where Step 1 resets  $z_t$  to  $\mathcal{M}^*$  at every cycle, this asymptotic statement is strengthened to a uniform bound holding from  $t = 0$ ; see Proposition 3.*

## B.2 Feasibility Closure Under Lie Group Integration

**Assumption 4** (Bounded Manifold Curvature). *The principal curvatures of  $\mathcal{M}^*$  are bounded above by  $\kappa_{\max} < \infty$ . Furthermore, the feasibility radius  $\delta_{\text{feas}}$  (defined in Proposition 2) satisfies  $\kappa_{\max} \delta_{\text{feas}} \leq \frac{1}{4}$ , so that the nearest-point projection  $\Pi_{\mathcal{M}^*}$  is at most  $\frac{3}{2}$ -Lipschitz on the  $\delta_{\text{feas}}$ -tube around  $\mathcal{M}^*$ . This ensures that the off-manifold distance argument in the per-cycle guarantee of Proposition 2 and the second-fundamental-form bound in Proposition 3 remain valid.*

The previous results bound the *magnitude* of the latent deviation from  $\mathcal{M}^*$  but do not explicitly characterise when the *decoded* action  $D_u(z_t)$  remains feasible, nor do they address the impact of nonconvexity of the Pareto objective. The following proposition closes both gaps.

**Proposition 2** (Lie Group Feasibility Closure). *Suppose:*

- (i) (Training feasibility) *Every training sample in  $\mathcal{D}$  is generated by solving the multi-objective problem to feasibility, so  $\mathcal{M}^* \subseteq \{z \in \mathcal{Z} : \mathbf{f}(D_u(z)) \leq \mathbf{0}\}$ .*
- (ii) (Lipschitz decoder)  *$D_u$  is  $K_{D_u}$ -Lipschitz on  $\mathcal{Z}$  and  $\mathbf{f}$  is  $L_f$ -Lipschitz on  $\text{Im}(D_u)$ .*
- (iii) (Positive feasibility margin) *There exists  $\gamma_{\min} > 0$  such that for every  $z^* \in \mathcal{M}^*$ :  $\min_i[-f_i(D_u(z^*))] \geq \gamma_{\min}$  (all training-data actions lie strictly inside the feasible set with uniform slack  $\gamma_{\min}$ ).*  
*Remark on active constraints: For problems such as AC OPF where constraint-active solutions (e.g. thermal limits reached at the Pareto front) make  $\gamma_{\min} = 0$  at individual points, this condition is enforced in practice by interior tightening during data generation: constraints are tightened by a small margin  $\eta_{\text{tight}} > 0$  (e.g.  $\eta_{\text{tight}} = 0.01$  per unit) so that every training-data solution satisfies  $f_i(D_u(z^*)) \leq -\eta_{\text{tight}}$ , setting  $\gamma_{\min} = \eta_{\text{tight}} > 0$ . The resulting  $\delta_{\text{feas}} = \eta_{\text{tight}}/(L_f K_{D_u})$  is a design parameter that trades off feasibility margin against proximity to the true Pareto front.*
- (iv) (Bounded curvature) *Assumption 4 holds.*

Define the feasibility radius:

$$\delta_{\text{feas}} \triangleq \frac{\gamma_{\min}}{L_f K_{D_u}} > 0. \quad (88)$$

Then for any  $z \in \mathcal{Z}$  satisfying  $\|z - \Pi_{\mathcal{M}^*}(z)\| \leq \delta_{\text{feas}}$ , the decoded action is feasible:  $\mathbf{f}(D_u(z)) \leq \mathbf{0}$ .

In particular, if the velocity cap enforces  $V_{\max}\Delta t \leq \delta_{\text{feas}}/2$  and the Step 1 localization satisfies  $\|z_t - \Pi_{\mathcal{M}^*}(z_t)\| \leq \delta_{\text{loc}}$  with  $\delta_{\text{loc}} \leq \delta_{\text{feas}}/2$ , then  $\mathbf{f}(\mathbf{u}_t) \leq \mathbf{0}$  at every cycle.

**This result holds without any convexity assumption on  $\mathbf{f}$  or on the Pareto objective.**

*Proof.* Let  $z^* = \Pi_{\mathcal{M}^*}(z)$  be the nearest point on  $\mathcal{M}^*$  to  $z$ . By assumption (i),  $\mathbf{f}(D_u(z^*)) \leq \mathbf{0}$ , and by assumption (iii) the slack at  $z^*$  is at least  $\gamma_{\min}$ :  $f_i(D_u(z^*)) \leq -\gamma_{\min}$  for all  $i$ .

Using the Lipschitz chains of  $D_u$  and  $\mathbf{f}$ :

$$\begin{aligned} f_i(D_u(z)) &= f_i(D_u(z)) - f_i(D_u(z^*)) + f_i(D_u(z^*)) \\ &\leq L_f \|D_u(z) - D_u(z^*)\| + f_i(D_u(z^*)) \\ &\leq L_f K_{D_u} \|z - z^*\| - \gamma_{\min}. \end{aligned} \quad (89)$$

For  $\|z - z^*\| \leq \delta_{\text{feas}} = \gamma_{\min}/(L_f K_{D_u})$ :

$$f_i(D_u(z)) \leq L_f K_{D_u} \delta_{\text{feas}} - \gamma_{\min} = \gamma_{\min} - \gamma_{\min} = 0, \quad (90)$$

establishing feasibility.

For the per-cycle guarantee: after Step 1 localization,  $\|z_t - \Pi_{\mathcal{M}^*}(z_t)\| \leq \delta_{\text{loc}} \leq \delta_{\text{feas}}/2$ . The Lie group integration step moves  $z_t$  by at most  $V_{\max}\Delta t \leq \delta_{\text{feas}}/2$  (velocity cap), so the new point  $z_{t+1}$  satisfies:

$$\|z_{t+1} - \Pi_{\mathcal{M}^*}(z_{t+1})\| \leq \|z_{t+1} - \Pi_{\mathcal{M}^*}(z_t)\| \leq \|z_{t+1} - z_t\| + \|z_t - \Pi_{\mathcal{M}^*}(z_t)\| \leq V_{\max}\Delta t + \delta_{\text{loc}} \leq \delta_{\text{feas}}, \quad (91)$$

where the first inequality uses the fact that  $\Pi_{\mathcal{M}^*}(z_t) \in \mathcal{M}^*$  is a feasible candidate (the nearest point can only be closer), the second is the triangle inequality, and the last uses  $V_{\max}\Delta t \leq \delta_{\text{feas}}/2$  and  $\delta_{\text{loc}} \leq \delta_{\text{feas}}/2$ . Feasibility at  $z_{t+1}$  then follows from the first part of the proof.

The argument uses only the Lipschitz properties of  $D_u$  and  $\mathbf{f}$  and the training-data feasibility margin; it does not use convexity of the Pareto objective  $\mathbf{J}(\mathbf{u})$ , convexity of the feasible set  $\{\mathbf{f}(\mathbf{u}) \leq \mathbf{0}\}$ , or any special structure of the Lie group  $G$ .  $\square$

**Remark 12** (Nonconvex problems). *The Pareto front of a nonconvex multi-objective problem is itself non-convex in objective space, but the feasibility argument is entirely in constraint space  $\{\mathbf{f}(\mathbf{u}) \leq \mathbf{0}\}$ . Since GPC embeds Pareto-optimal solutions into  $\mathcal{M}^*$  regardless of the shape of the Pareto front, Proposition 2 applies verbatim to both the convex-objective and nonconvex-objective analytical benchmarks of Sections 5.1 and 5.2, as well as to the nonconvex AC power flow feasibility manifold of Section 5.3.*

### B.3 Closed-Loop Non-Accumulation via Step 1 Reset

Proposition 1 and Theorem 1 bound the steady-state latent drift of the *free-running* integrator via a contractive fixed point. Algorithm 1 goes further: Step 1 localization re-anchors  $z_t$  to  $\mathcal{M}^*$  at *every* cycle, preventing drift from any single cycle from propagating into the next. The following proposition formalises this *uniform* (non-asymptotic) non-accumulation under two idealized assumptions: that the Step 1 reset is exact, and that the post-reset flow velocity is tangential to  $\mathcal{M}^*$ .

**Assumption 5** (Tangential Post-Reset Flow). *After the Step 1 hard reset  $z_t \leftarrow z_t^{\text{loc}} \in \mathcal{M}^*$ , the integration velocity used in Algorithm 1 is the Riemannian gradient of  $\Phi_{\text{tangent}}$  projected onto  $T_{z_t}\mathcal{M}^*$ :*

$$\dot{z}_{\text{safe},t} = -\Pi_{T_{z_t}\mathcal{M}^*}(\nabla_z \Phi_{\text{tangent}}(z_t)), \quad (92)$$

where  $\Pi_{T_z\mathcal{M}^*}$  denotes orthogonal projection onto the tangent space at  $z$ . This ensures  $\dot{z}_{\text{safe},t} \in T_{z_t}\mathcal{M}^*$ , so that the Lie group exponential step departs tangentially and the off-manifold deviation is purely second-order in  $\Delta t$ . In practice this projection is approximated by the Riemannian gradient computed via the metric induced by  $D_s$ ; without this projection, the Euclidean gradient  $\nabla_z \Phi_{\text{tangent}}$  has a nonzero normal component and the  $O(\kappa V^2 \Delta t^2)$  first-order tangentiality claim does not hold.

**Assumption 6** (Exact Closed-Loop Re-anchoring). *At the start of each control cycle  $t$ , the Step 1 localization procedure returns a point  $z_t^{\text{loc}} \in \mathcal{M}^*$  satisfying  $\|z_t - z_t^{\text{loc}}\| \leq \delta_{\text{loc}}$ , and the latent state is hard-reset to  $z_t \leftarrow z_t^{\text{loc}}$  before the integration step is applied.*

**Proposition 3** (Uniform Closed-Loop Non-Accumulation). *Let  $\delta_{\text{loc}} > 0$  be the localization error of Step 1, satisfying  $\|z_t - \Pi_{\mathcal{M}^*}(z_t)\| \leq \delta_{\text{loc}}$  for all  $t \geq 0$ , and let  $\delta_{\text{loc}}$  be calibrated from the held-out loss  $\mathcal{L}_{\text{local}}^{\text{val}}$  via the geometric tolerance  $\tau_{\text{geom}}$ . Then under the conditions of Theorem 1, Assumption 4, Assumption 5, and Assumption 6:*

$$\sup_{t \geq 0} \|\mathbf{u}_t - \mathbf{u}_t^*\| \leq K_{D_u} (\delta_{\text{loc}} + \frac{1}{2} \kappa_{\text{max}} V_{\text{max}}^2 \Delta t^2) + \delta_{\text{dec}}. \quad (93)$$

The bound is **uniform in  $t$** , holds from cycle  $t = 0$ , and does not depend on any limit or fixed-point argument.

*Proof.* By Assumption 6, at the start of each cycle  $t$ , Step 1 localization provides  $z_t^{\text{loc}} \in \mathcal{M}^*$  with:

$$\|z_t - z_t^{\text{loc}}\| \leq \delta_{\text{loc}}, \quad z_t \leftarrow z_t^{\text{loc}}. \quad (94)$$

This is a hard reset: the latent state is replaced by its nearest point on  $\mathcal{M}^*$  at the start of every cycle, so any off-manifold error from the previous cycle is discarded before the new integration step begins.

Starting from  $z_t^{\text{loc}} \in \mathcal{M}^*$  (off-manifold distance zero after the reset), we show the Lie group integration step moves  $z_t^{\text{loc}}$  *tangentially* to  $\mathcal{M}^*$  to first order. Since  $z_t^{\text{loc}} \in \mathcal{M}^*$ , the normal potential  $\Phi_{\text{normal}}(z_t^{\text{loc}}) = 0$ , so  $\nabla_z \Phi_{\text{normal}}(z_t^{\text{loc}}) = 0$  (the snap gradient vanishes exactly on  $\mathcal{M}^*$ ). By Assumption 5,  $\dot{z}_{\text{safe},t} = -\Pi_{T_{z_t}\mathcal{M}^*}(\nabla_z \Phi_{\text{tangent}}(z_t^{\text{loc}}))$  is a purely tangential velocity  $\dot{z}_{\text{safe},t} \in T_{z_t^{\text{loc}}}\mathcal{M}^*$ . A Lie group exponential step by a tangent vector  $v \in T_z\mathcal{M}^*$  stays on  $\mathcal{M}^*$  to *first order* and deviates by  $O(\|v\|^2 \Delta t^2)$  due to curvature of  $\mathcal{M}^*$  (the second fundamental form argument: the normal component of the geodesic deviation is  $\frac{1}{2} \Pi(v, v) \Delta t^2$ ). Therefore, with  $\|v\| \leq V_{\text{max}}$  and  $\kappa$  the curvature bound:

$$\|z_{t+1} - \Pi_{\mathcal{M}^*}(z_{t+1})\| \leq \frac{1}{2} \kappa_{\text{max}} V_{\text{max}}^2 \Delta t^2, \quad (95)$$

where  $\kappa_{\text{max}}$  is the curvature bound from Assumption 4. After the next cycle's Step 1 reset, the off-manifold distance returns to  $\leq \delta_{\text{loc}}$ , independent of  $t$ . Therefore, for all  $t \geq 0$ :

$$\|z_t - z_t^*\| \leq \delta_{\text{loc}} + \frac{1}{2} \kappa_{\text{max}} V_{\text{max}}^2 \Delta t^2, \quad (96)$$

---

where  $z_t^* = \Pi_{\mathcal{M}^*}(z_t^{\text{loc}})$  is the nearest Pareto-optimal point. Applying the  $K_{D_u}$ -Lipschitz decoder and the triangle inequality (as in Stage 4 of the proof of Theorem 1):

$$\begin{aligned} \|\mathbf{u}_t - \mathbf{u}_t^*\| &\leq K_{D_u} \|z_t - z_t^*\| + \delta_{\text{dec}} \\ &\leq K_{D_u} (\delta_{\text{loc}} + \frac{1}{2} \kappa_{\text{max}} V_{\text{max}}^2 \Delta t^2) + \delta_{\text{dec}}. \end{aligned} \tag{97}$$

Since the right-hand side is independent of  $t$ , the supremum over all  $t \geq 0$  is finite and equal to the expression in (93).  $\square$

**Remark 13** (Comparison with Proposition 1 and Theorem 1). *Proposition 1 establishes a lim sup bound that requires infinite time to approach and relies on a Banach fixed-point argument for the free-running integrator. Proposition 3 replaces this with a sup bound that holds from  $t = 0$ , using only a one-step induction made possible by the Step 1 reset. The two results are complementary: Proposition 1 characterises the integrator in isolation; Proposition 3 characterises the full closed-loop algorithm and is the stronger, operationally relevant statement. Note that  $\delta_{\text{loc}}$  is an additional tunable parameter (controlled by  $\tau_{\text{geom}}$ ) that is absent from Theorem 1; reducing  $\tau_{\text{geom}}$  tightens the localization error at the cost of a smaller feasible localization set  $\mathcal{M}_t$ .*